Hybrid Polymer Plasmonic Devices for Enhanced All-Plasmonic Switching Based on Photothermal Nonlinearity

by

David Harwood Perron

A thesis submitted in partial fulfillment of the
requirements for the degree of

Master of Science
in
Photonics and Plasmas

Department of Electrical and Computer Engineering
University of Alberta

Abstract

Nanoplasmonic devices have received much attention in recent years due to their ability to confine light below the diffraction limit, thereby providing a potential route to the creation of nanometer-scale integrated photonic devices. However, with the strong confinement of light come large absorption losses and the resulting joule heating in the metal layers. This conversion of light into heat can have significant impact on the device performance as material properties change. On the other hand, it can also give rise to large photothermal effects which can be exploited for nonlinear device applications.

This thesis explores the possibilities of exploiting the strong photothermal nonlinearity associated with the absorption of light in plasmonic devices for all-plasmonic switching applications. A hybrid plasmonic waveguide based on a polymer material is proposed and designed to achieve strong photothermal nonlinear effects. It is found that the large absorption in the plasmonic waveguide leads to a thermo-optic change in the material's refractive index that is two orders of magnitude greater than in a similar photonic waveguide structure. The strong photothermal nonlinearity is exploited in the creation and experimental demonstration of an all-plasmonic switching device based on an all-pass microring resonator.

Acknowledgements

The completion of this thesis wouldn't have been possible without my supervisor, Dr. Vien Van. His advice, support and encouragement gave me the motivation to push through my many difficulties along the way. He has my deepest gratitude in giving me the opportunity to study under him.

A great deal of support came from among my colleagues at the Nanophotonics Research Laboratory. I would especially like to give appreciation to Ashok Prabhu Masilimani for his insights and thought-provoking discussions on the nature of photonics and many other topics. Daniel Bachman, Cameron Horvath, Rice Mi, Alan Tsay, Siamak Abdollahi and Marcelo Wu also helped to relieve the stress of graduate life in our lab in addition to our technical discussions, for which I thank them dearly.

Finally, and most importantly, I wish to thank my friends and family, especially my parents and my wife Andrea, for being with me on every step of this journey.

Table of Contents

List of Figures

List of Tables

List of Symbols

I	intensity of electromagnetic wave [W / m^2]
z	distance in direction of propagation [m]
L_p	propagation distance of waveguide [m]
λ	wavelength of electromagnetic wave [m]
R	radius of microring [m]
$\tilde{n}$	complex refractive index of a material (dimensionless)
n	real part of the refractive index (dimensionless)
κ	imaginary part of the refractive index (dimensionless)
$\tilde{n}_{eff}$	complex effective index of a waveguide (dimensionless)
ς	field coupling coefficient (dimensionless)
τ	field transmission coefficient (dimensionless)
S_i	input port optical signal [V / m]
S_t	output port optical signal [V / m]
α_{rt}	microring roundtrip attenuation factor (dimensionless)
α_{c}	coupling attenuation factor (dimensionless)
T_{ap}	normalized throughput power (dimensionless)
ϕ_{rt}	roundtrip phase [radians]
$\frac{dn}{dT}$	thermo-optic coefficient of material [K^{-1}]
T	temperature [K]
K	thermal conductivity [W / m·K]
q"	rate of heat generation [W / m^3]

$\boldsymbol{f}$	force density on charge distribution [N / m^3]
ρ	charge density of charge distribution [C / m^3]
$\boldsymbol{v}$	velocity of charge distribution [m / s]
$\boldsymbol{E}$	electric field strength [V / m]
$\boldsymbol{B}$	magnetic flux density [N / A·m]
$\boldsymbol{H}$	magnetic field strength [A / m]
W	kinetic energy [J]
$\boldsymbol{J}$	current density [A / m^2]
σ	electrical conductivity [S / m]
$\tilde{\chi}_e$	complex electrical susceptibility (dimensionless)
χ_m	magnetic susceptibility (dimensionless)
ε_o	permittivity of free space [F / m]
ω	angular frequency of electromagnetic wave [radians / s]
$\tilde{\varepsilon}$	complex permittivity of medium [F / m]
$\tilde{k}$	complex vacuum wavenumber [radians / m]
α	absorption coefficient [m^{-1}]
P_i	microring input power [dBm]
P_f	fiber input power [dBm]
P_{out}	fiber output power [dBm]
l_f	fiber-to-waveguide coupling loss [dB]
l_c	photonic-to-plasmonic waveguide coupling loss [dB]
l_{ph}	photonic waveguide propagation loss [dB]
l_{pl}	plasmonic waveguide propagation loss [dB]
α_{L_p}	propagation loss per unit length [dB/m]
l_p	overall propagation loss [dB]

1 Introduction

1.1 Background motivation

Fiber optics have long replaced electrical wires in long distance communications due to the much larger data transmission bandwidths they can provide compared to electrical cables. However, much of the information processing functionalities, such as switching, modulation and demodulation, are still being handled by electronic circuits which, due to their speed limitation, are now becoming a serious bottleneck in high-speed data transmission links [1]. Photonic integrated circuits (PICs), which perform signal processing directly on the optical data streams, offer a potential solution to the electronic bottleneck problem. As such, interest in the development of PICs and their incorporation into, or even replacement of, electronic integrated circuits continues to rise [2, 3]. Implementations of multi-layer combinations of electronics and PICs are in development by industry leaders like Intel [4] and IBM [5]. However, there are still significant challenges to the practicality of PICs for very large scale applications.

One primary concern is that of size. Current state-of-the-art transistors have reached features sizes of around 30nm, while the smallest traditional

photonic features are an order of magnitude larger. This is because light cannot be confined below the diffraction limit of light (about half of a wavelength) in a conventional dielectric waveguide. This leads to large mismatches between combined photonic/electronic integration and presents a major barrier to the replacement of electronic circuitry with photonics. The field of integrated plasmonics offers a possible solution for reducing photonic components to the scale of electronics [6, 7]. With the addition of metal layers to standard dielectric or semiconductor waveguides, interactions between the confined light and free carriers in the metal are induced, leading to electromagnetic waves with high intensities at the metal-dielectric interfaces. Various waveguide configurations allow for large field concentration to exist within subwavelength dimensions at these interfaces, hence bypassing the diffraction limit of standard photonic waveguides. A brief discussion on the basics of plasmonics, several waveguide architectures, and the effects of propagation loss are included in section 1.2.

One issue with plasmonic waveguides is that the high intensity at the metal interface results in absorption losses as heat due to field penetration into the metal layer. The extent of this loss is modified by the wave's confinement, with stronger confinement resulting in larger loss. An important effect of absorption is that the heat generated from joule heating in the metal layers can cause thermo-optic changes to the material properties, with potential consequences for device performance. In some cases, these consequences are detrimental enough that steps are taken specifically to counteract the changes [8]. This thesis will instead demonstrate how the thermo-optic changes can be utilized beneficially.

Electronic integrated circuits have a basic building block for their devices in the transistor. No such universal component yet exists for photonic devices, so PICs must be individually designed to achieve desired functionalities. One type of component that has been used as a photonic building block is the microring resonator (MRR), due to its versatile spectral characteristics. These components have been used in numerous integrated applications such as optical switches [9] and filters [10], slow light [11], and delay lines [12]. An important characteristic of the MRR is that it can provide large electromagnetic field enhancement at resonant frequencies, which have been used to exploit the various nonlinearities of device materials. Similar to how transistors allow for one electrical signal to control another, the large nonlinear effects in an MRR, combined with its spectral characteristics, can be used to control one light signal with another. Examples of nonlinear phenomena range from relatively slow photothermal nonlinearity (μs-ms) [13], to the faster effects of two-photon absorption [14] and free carrier dispersion (ps-ns) [15], to the ultrafast phenomena of Kerr nonlinearity (fs) [16]. Although the slowest, photothermal nonlinearity is also frequently the strongest in a material, and generally, the easiest to induce. As mentioned previously, photothermal nonlinearity is especially pronounced in a plasmonic waveguide due to the large heat generated from absorption in the metal layers, which can be exploited for device applications in active plasmonic control. MRRs are discussed in some detail in section 1.3, and photothermal nonlinearity will be described in depth in Chapter 2.

While there is a great deal of interest in silicon-based and similar inorganic material platforms for PICs due to their potential for integration into

mature electronic chip-based manufacturing processes [17], there are applications where the use of polymer-based platforms is preferable despite their large dimensions, such as biochemical sensing [18, 19] or optical microfluidics integration [20]. Polymers are relatively simple and inexpensive to process [21], easy to dope for sensing and nonlinear purposes [18, 22, 23], and have otherwise useful mechanical, electro-optic and thermo-optic properties [24] for photonic devices. These qualities have led to proposals and demonstrations of polymer-based optical interconnects and other PICs [19, 25, 26]. SU-8 is a popular polymer used in many different microtechnology-based applications. As a type of photoresist, it is often used as an intermediate layer in the device fabrication process. However, unlike other photoresists which are removed during the course of fabrication, SU-8 becomes permanent when processed [27]. This, in conjunction with advantageous properties such as rigidity, chemical stability, and low cellular toxicity has led to its use in microelectromechanical systems [28], microfluidics [29], and bio/chemical sensing [30]. For optical applications, its permanency, simplicity of manufacture, low cost and high transparency at telecommunication wavelengths have made it a widely used platform for passive and active devices [24, 31]. SU-8 also has a strong thermo-optic coefficient, and as such, its refractive index is highly temperature sensitive. This makes it an excellent material for use in a photothermal nonlinearity-based active device.

This work focuses on maximizing the effects of photothermal nonlinearity in a plasmonic waveguide, disregarding considerations of reduced photonic/plasmonic feature sizes. Given the above background motivation, the thesis aims to demonstrate substantially increased photothermal nonlinear

effects in plasmonic devices over similar photonic device structures. In addition to theoretical and numerical calculations, an optically controlled microring switch is fabricated to experimentally demonstrate the extent and effect of heat generation in temperature sensitive plasmonic PICs.

Section 1.2 gives a brief overview of the field of plasmonics, focusing on the subjects investigated in this work, and section 1.3 introduces the all-pass microring device used to demonstrate all-plasmonic switching based on photothermal nonlinearity, the microring device to be demonstrated as a switch. The final section in this chapter contains the outline and objective for the rest of the thesis. Note that all discussion throughout the thesis takes place around the telecommunications wavelength of 1550nm.

1.2 Surface plasmon polaritons and plasmonic waveguide architectures

Surface plasmon polaritons (SPPs) are coherent electron oscillations that are created by an electromagnetic wave as it interacts with a metal surface, or more generally, as it propagates along any two materials whose real permittivities have opposite signs (as is generally the case for dielectrics and metals) [32]. The SPPs propagate as part of the electromagnetic mode, with the field intensity maximized at the metal-dielectric interface. As illustrated in figure 1.1, the field decays exponentially as it extends away from the interface, with a much steeper rate on the metal side [33]. The dielectric side of the interface exhibits a slowly decaying tail that can extend far away from

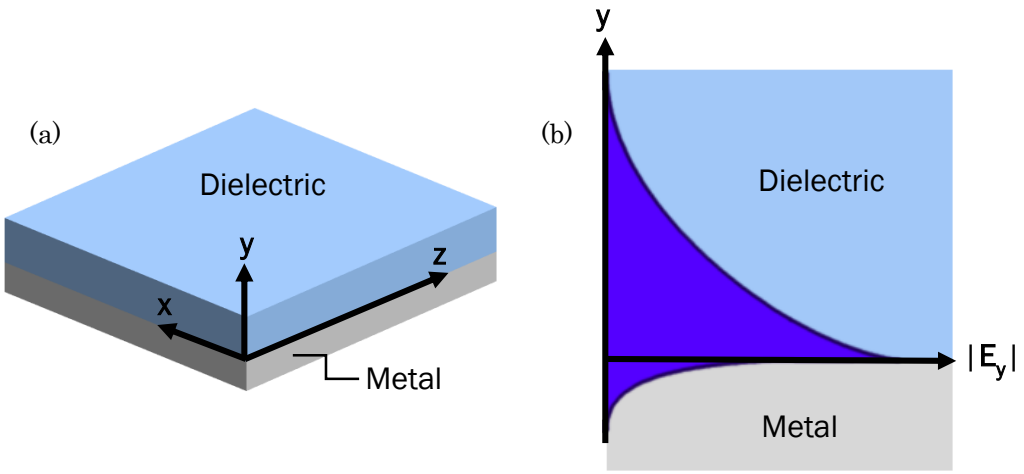

Fig. 1.1: (a) Geometry of the metal-dielectric interface. (b) Depiction of the dominant component of the electric field as the wave propagates in the z-direction along the dielectric-metal interface.

the metal-dielectric interface. The field that penetrates into the metal is subject to the metal's absorption losses and is the primary contributor to loss in the plasmonic waveguide. The dominant field is always perpendicular to the metal-dielectric interface plane.

Due to the high loss inherent in plasmonic waveguide, it becomes important to quantify the propagation length L_p of a given supported plasmonic mode. This defines the distance a wave will travel in a given architecture before its intensity I drops by $1/e$ of its original intensity I_o:

$$I = I_o e^{-z/L_p}, \tag{1.1}$$

where z is the distance traveled by the wave in the propagating direction.

A plasmonic structure with a simple metal-dielectric interface like the one shown above can have a propagation length in the range of millimeters. By coupling an additional SPP mode at a second identical metal-dielectric interface on the other side of a very thin metal layer, the two modes can be combined such that there is reduced field present inside the metal. This

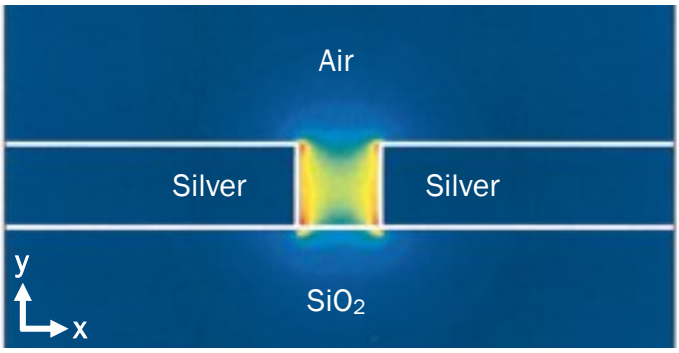

Fig. 1.2: Power density profile of the fundamental mode of the metal-dielectric-metal waveguide [35], propagating in the z-direction. The metal height and gap width are roughly 50nm.

extends the propagation length to the centimeter scale. These so-called long-range SPP modes in a dielectric-metal-dielectric (DMD) plasmonic structure have some of the longest propagation lengths known in plasmonics, at the expense of very loose mode confinement [34].

Alternatively, high mode confinement can be created by adding a second metal-dielectric interface and form a metal-dielectric-metal waveguide [35]. This cuts off the slowly decaying dielectric tail to convert it into another peak at the second interface as can be seen in figure 1.2 with a two dimensional waveguide. The highly localized SPPs on the two interfaces imply tremendous loss. Typical propagation lengths for these devices are limited to 10-15μm [36, 37].

Simply adding two-dimensional boundaries to the dielectric medium to form the shape and size of a standard dielectric waveguide with a metal layer results in severe reductions in propagation lengths as well, on the order of 2-40μm [38, 39], which increases with larger dielectric cores. Propagation lengths can be increased significantly with the simple addition of a second lower-index dielectric between the metal and higher index dielectric core. The

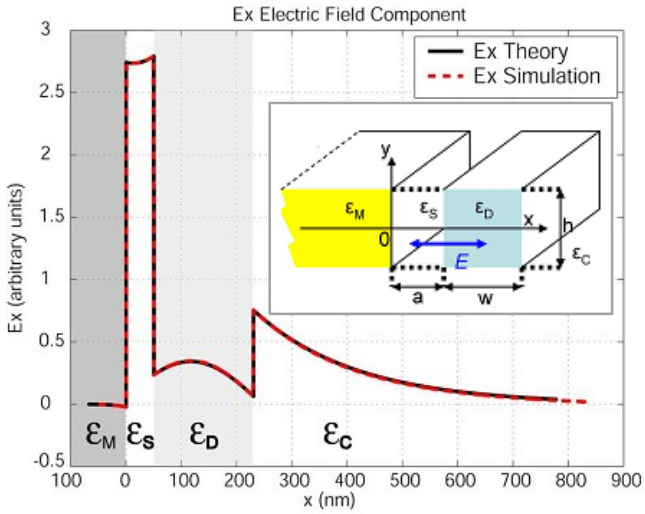

Fig. 1.3: Dominant component of the electric field distribution of a hybrid plasmonic waveguide, seen from an x-axis cross-section. Permittivitty of material $\varepsilon_D > \varepsilon_S$ and ε_C, with ε_M as a metal [40]. Inset: hybrid plasmonic waveguide geometry.

addition of this low index gap layer between the core and metal has been proposed and demonstrated to good effect [40, 41]. High mode confinement exists in the low index material as shown in figure 1.3 due to a combination of plasmonic and high-index contrast (or purely photonic) effects. Outside of the high-confinement area in the higher index dielectric, a semi-photonic mode is formed reducing the amount of field in close proximity of the metal interface. These effects allow for relatively strong interaction with the metal layer while still producing propagation lengths from 10s to 100s of microns. The structure of the hybrid plasmonic waveguide allows for simple integration with pure photonic bus waveguides, thus helping to reduce the overall device loss. The balance between confinement and propagation length is particularly important in the design of a plasmonic MRR. The higher confinement allows for reduced bending loss, while a longer propagation length allows for increased interaction with the resonator.

The hybrid plasmonic waveguide used in this work is characterized in depth in Chapter 3. As the focus of this work is on the hybrid plasmonic waveguide, the rest of this thesis uses the terms "hybrid plasmonic" and "plasmonic" interchangeably.

1.3 The all-pass microring filter

The all-pass microring filter is one of the simplest integrations of a microring resonator into a photonic device. It consists of a microring positioned next to a single bus waveguide, and has one each of input and output ports, as shown in figure 1.4. A portion of the input electromagnetic field S_i couples into the microring, where it then travels around until it reaches the coupler again. A portion then leaves the microring and couples back into the waveguide. The throughput field S_t is the sum of the input field and the field coupled out of the microring. At resonance wavelengths λ_m, the field inside the ring constructively interferes with itself, resulting in a large buildup of field and energy. This is known as field enhancement. Resonance occurs whenever an

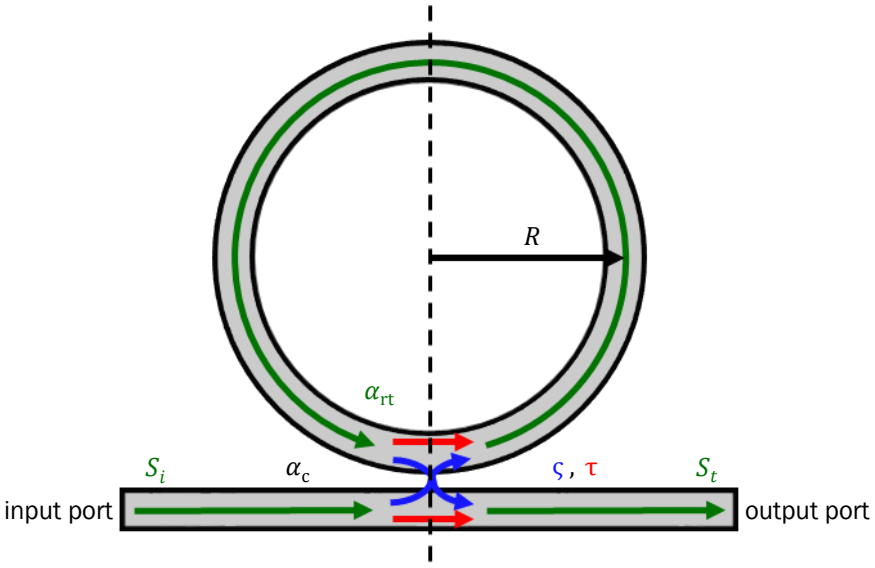

Fig. 1.4: Schematic of an all-pass microring filter of radius R with coupling and transmission coefficients ς and τ, coupling loss α_c, and roundtrip loss α_{rt}.

integer multiple m of the guided field's wavelength is equal to the roundtrip path length of the microring:

$$\frac{\lambda_m}{n_{eff}} = \frac{2\pi R}{m} \tag{1.2}$$

where n_{eff} is the effective index seen by the field mode and R is the radius at which the field travels through the ring. The spacing between two consecutive resonances is known as the resonator's free spectral range. It can be seen from equation 1.2 that this spacing is not constant between resonances, as n_{eff} is wavelength-dependent.

Power couples in and out of the resonator via a coupling junction with coupling coefficient ς between the ring and waveguide, with a portion of it bypassing the microring as determined by the transmission coefficient τ. The total input intensity $|S_i|^2$ is thus divided between the output port and microring such that $(\varsigma^2 + \tau^2)|S_i|^2 = |S_i|^2$.

With many waveguide architectures, particularly plasmonics as discussed above, notable loss occurs as the field travels. The roundtrip field attenuation factor α_{rt} denotes the fraction of the field remaining after one complete roundtrip. The coupling junction between microring and waveguide is also a source of loss. Traditional photonic MRRs utilize evanescent coupling between waveguides [10], where power transfer occurs via the waveguides' evanescent fields. This allows for negligible loss and small coupling strengths. In situations where increased coupling is desired, such as between strongly-confined waveguides or in MRRs with high roundtrip loss (as with a plasmonic MRR), a multimode interference (MMI) coupler is useful. In an MMI coupler, the physical connection between two adjoined waveguides allows for direct

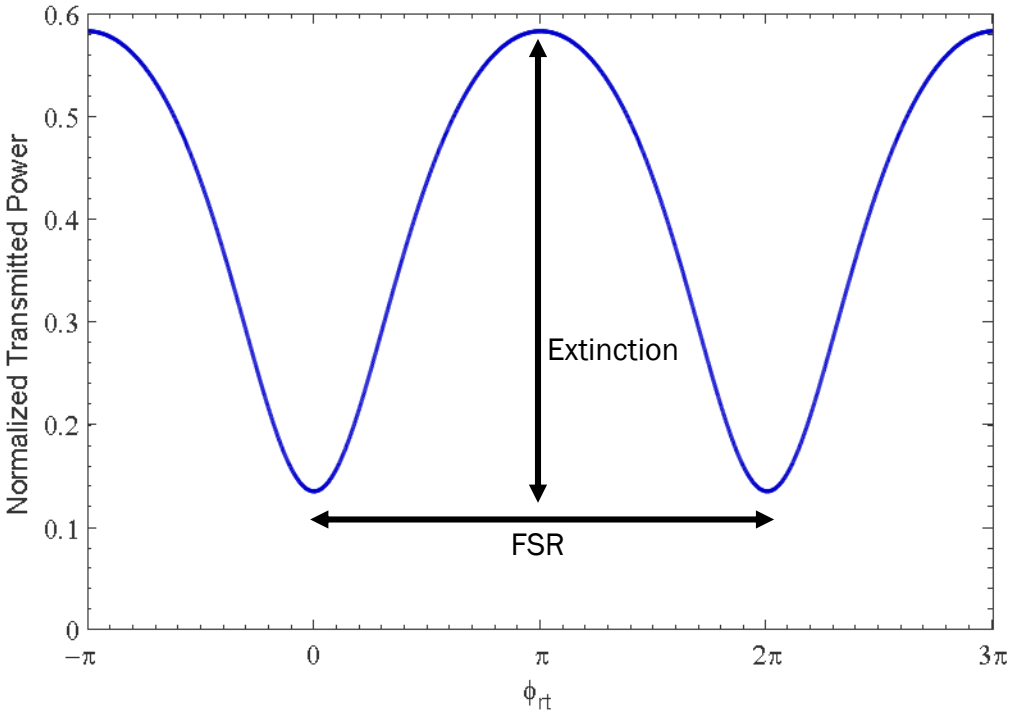

Fig. 1.5: Spectral response of the normalized transmitted power P through an all-pass MRR with 50% coupling ($\varsigma^2 = 0.5$), 84% roundtrip loss ($a_{\mathrm{rt}} = 0.3$) and 39% coupling loss ($a_{\mathrm{c}} = 0.85$).

interaction between the separate waveguide modes, and can result in high power transfer over short distances. However, MMI couplers have noticeable loss associated with them [42]. In these cases, a coupling attenuation factor α_{c} is included in formulations.

The spectral response of the normalized throughput power T_{ap} at the output port is obtained with [43]:

$$T_{\mathrm{ap}} = \left|\frac{S_t}{S_i}\right|^2 = \frac{{\alpha_{\mathrm{c}}}^2\tau^2 + {\alpha_{\mathrm{rt}}}^2 - 2\alpha_{\mathrm{rt}}\alpha_{\mathrm{c}}\tau\cos\phi_{\mathrm{rt}}}{1 + {\alpha_{\mathrm{rt}}}^2{\alpha_{\mathrm{c}}}^2\tau^2 - 2\alpha_{\mathrm{rt}}\alpha_{\mathrm{c}}\tau\cos\phi_{\mathrm{rt}}} \tag{1.3}$$

where $\phi_{\mathrm{rt}} = 4\pi^2 n_{eff}\lambda R$ is the roundtrip phase of the microring. Figure 1.5 shows a sample spectral response for T_{ap}. At resonances, when the input signal wavelength λ matches λ_m and thus $\phi_{\mathrm{rt}} = 2m\pi$, the transmission experiences a dip as the signal leaving the microring works to partially cancel out the input

signal through destructive interference. Minimum and maximum (off-resonance) transmission powers are thus given by:

$$T_{\text{ap, min}} = \left(\frac{\alpha_c \tau - \alpha_{rt}}{1 - \alpha_{rt}\alpha_c \tau}\right)^2, \tag{1.4}$$

$$T_{\text{ap, max}} = \frac{{\alpha_c}^2 \tau^2 + {\alpha_{rt}}^2}{1 + {\alpha_{rt}}^2 {\alpha_c}^2 \tau^2}. \tag{1.5}$$

Dividing equation 1.4 by equation 1.5 gives the resonator's extinction ratio. High extinction can be found despite large loss as $\alpha_c \tau$ approaches the value of α_{rt}. High extinction ratios are desirable in active devices based on all-pass MRRs, as will be shown in Chapter 5. Note in 1.4 that if α_c and α_{rt} both equal 1 (no loss), there is zero attenuation in the transmitted power at all wavelengths. For this reason, the MRR structures is called an all-pass filter.

1.4 Research objectives and thesis organization

The aim of this thesis is to explore and utilize the strong photothermal effects in plasmonic devices. The thesis proposes and designs a hybrid plasmonic waveguide platform based on the polymer material SU-8. The photothermal nonlinear effects of this waveguide design are investigated. A fabricated hybrid plasmonic microring resonator based on the waveguide design is used to exploit photothermal nonlinearity to experimentally demonstrate all-plasmonic switching.

This thesis contains five additional chapters, all of which focus on the effects of thermal nonlinearity on materials and active devices. The layout is as follows:

- Chapter 2 develops the equations that govern how a material's refractive index changes with the absorption of heat. Included is a

detailed analysis of how a guided wave's electromagnetic field is absorbed by the material it passes through.

- Chapter 3 includes numerical simulations to study the specific propagation and heat production characteristics of a chosen hybrid plasmonic waveguide structure.
- Chapter 4 describes the fabrication process that was used to create the hybrid plasmonic waveguides and device to be experimentally characterized.
- Chapter 5 presents the linear and nonlinear characterization of a hybrid plasmonic all-pass filter. In addition, its use as a photothermal switch is demonstrated.
- Chapter 6 provides a summary of the work and suggests further research directions.

2 Thermo-Optic Relations

This chapter details the equations used to describe temperature change in a material due to a heat source, and the refractive index shift caused by the change in temperature. It then formulates the relevant equations used to show how electromagnetic waves inside a lossy guiding structure get absorbed to generate heat. Finally, several methods to convert between different material absorption parameters are shown, as to allow the use of parameter measurements from various reference sources.

The nature of the experiments in Chapter 5 allows several simplifications to be made throughout this chapter. The measurements will be taken at steady state, so any time dependence can be removed. In addition, the materials used are not magnetic, so contributions due to magnetism are not included.

2.1 Thermo-optic effect

Refractive index shift due to temperature is generally linear over small ranges. As such, the change in a material's refractive index Δn can be determined by the following equation:

$$\Delta n = \frac{dn}{dT}\Delta T, \tag{2.1}$$

where dn/dT is the material's thermo-optic coefficient and ΔT is the material's

change in temperature. In the case of the thermo-optic waveguide, the source of this temperature change is the heat generated by the absorption of light propagating through the waveguide, which is then conducted throughout the material system. The steady state relationship between the heat generated and the system's temperature is given by the heat equation:

$$\nabla \cdot (K\nabla T) = -q''. \tag{2.2}$$

The thermal energy generation rate q'' describes the rate at which heat enters the material system, while the material's thermal conductivity K determines the ability for heat to spread through the different materials. Solving for T results in a temperature distribution that can then be used in equation 2.1 to find the modified refractive index of the material system.

2.2 Material losses due to charge excitation

Many materials are essentially transparent in a certain frequency range, and light will pass through them with negligible reduction in power. For example, silicon dioxide is transparent at wavelengths around 1550nm, which makes it an ideal material for use in long-distance fiber optics.

Materials that begin absorbing energy from the light waves do so in a number of ways. Good conductors have free charges that conduct energy from the electric field away to produce a current while good dielectrics have bound charges that will absorb energy to polarize in response to the electric field. Magnetic materials can also cause loss by drawing energy away from a wave's magnetic field, but as the materials used in the SU-8 plasmonic waveguide are magnetically inert, these losses are negligible.

The electromagnetic field exerts a force on these charges, increasing their

kinetic energy, which eventually dissipates as heat. This force is known as the Lorentz Force, and the equation:

$$\boldsymbol{f} = \rho\left(\boldsymbol{E} + \boldsymbol{v} \times \boldsymbol{B}\right) \tag{2.3}$$

describes the force per unit volume $\boldsymbol{f}$ on a charge distribution ρ moving at a velocity $\boldsymbol{v}$ due to due to electric field $\boldsymbol{E}$ and magnetic field $\boldsymbol{B}$. The kinetic energy W gained by the charge distribution is then:

$$W = \iint \boldsymbol{f} \cdot \boldsymbol{v} dt dV. \tag{2.4}$$

Note that this equation shows that since the force due to the magnetic field is perpendicular to the movement of the particles, in which $(\boldsymbol{v} \times \boldsymbol{B}) \cdot \boldsymbol{v} = 0$, only the electric field contributes to the increase in kinetic energy.

2.3 Current density in materials

A distribution of free charges, polarizable charges and magnetic dipoles will have a current density of:

$$\boldsymbol{J} = \rho \boldsymbol{v}, \tag{2.5}$$

The charge distribution inside of a material can be quantified by three material properties: electrical conductivity σ, describing the material's ability to conduct free charges, its complex electrical susceptibility $\tilde{\chi}_e$, describing the ability for its bound charges to polarize, and its magnetic susceptibility $\tilde{\chi}_m$, describing the material's ability to magnetize. The current density in a material with both free and bound charges is:

$$\boldsymbol{J} = \sigma \boldsymbol{E} + \varepsilon_o \tilde{\chi}_e \frac{\partial \boldsymbol{E}}{\partial t} + \nabla \times \tilde{\chi}_m \boldsymbol{H}, \tag{2.6}$$

where ε_o is the permittivity of free space and $\boldsymbol{H}$ is the wave's magnetic field strength. The terms on the right hand side are due to free charges, polarizable

charges and magnetic dipoles, respectively. Note that magnetically inert materials have $\tilde{\chi}_m$ that are effectively zero, and therefore only a wave's electric field contributes to $\boldsymbol{J}$ in these materials. As this thesis deals with only magnetically inert materials, the last term in equation 2.6 is ignored.

Equations 2.3 through 2.5 can be combined to form:

$$W = \iint \left(\boldsymbol{J} \cdot \boldsymbol{E} + \boldsymbol{v} \cdot \boldsymbol{v} \times \boldsymbol{B}\right) dtdV. \tag{2.7}$$

After accounting for the magnetic field being perpendicular to the particle movement, equation 2.7's dependence on the charge distribution's ρ and $\boldsymbol{v}$ can be completely replaced by the material's properties conductivity σ and electric susceptibility χ_e in equation 2.6. Differentiating the equation in terms of time and volume results in a much simplified relation:

$$\frac{\partial^2 W}{\partial t \partial V} = \boldsymbol{J} \cdot \boldsymbol{E}. \tag{2.8}$$

This equation is the power expended by the fields to move the charges per unit volume, dispersing as heat: the time transient form of q'' in equation 2.2.

2.4 Guided travelling waves

The charge distribution's kinetic energy is a real value. However, a continuous guided wave with time dependence $e^{-i\omega t}$ is best described using complex notation:

$$\boldsymbol{E} = Re\{\widetilde{\boldsymbol{E}}\} = Re\{\widetilde{\boldsymbol{E}}_o e^{-i\omega t}\}, \tag{2.9}$$

where $\widetilde{\boldsymbol{E}}_o$ describes the field's spatial characteristics, and angular frequency ω. Using the property $Re\{\widetilde{\boldsymbol{E}}\} = (\widetilde{\boldsymbol{E}} + \widetilde{\boldsymbol{E}}^*)/2$, where $\widetilde{\boldsymbol{E}}^*$ is the complex conjugate of $\widetilde{\boldsymbol{E}}$, equation 2.8 can be solved as:

$$\frac{\partial^2 W}{\partial t \partial V} = \frac{1}{4}\left(\tilde{\boldsymbol{J}} + \tilde{\boldsymbol{J}}^*\right) \cdot \left(\widetilde{\boldsymbol{E}} + \widetilde{\boldsymbol{E}}^*\right), \tag{2.10}$$

with $\tilde{\boldsymbol{J}}$ a function dependent on $\widetilde{\boldsymbol{E}}$.

The electric susceptibility $\tilde{\chi}_e$ is complex, with its real part indicating the material's ability to store energy in a given electric field, and its imaginary part indicating the dissipation of energy with the material's inability to polarize instantaneously with quickly changing fields. This imaginary component is therefore similar to the material's conductivity σ, which describes energy loss due to the excitation of its free charges. Accounting for this and equation 2.9, equation 2.6 can be transformed into:

$$\tilde{\boldsymbol{J}} = -i\omega(\varepsilon_1 + i\varepsilon_2 - \varepsilon_o)\widetilde{\boldsymbol{E}} \tag{2.11}$$

where $\varepsilon_1 = \varepsilon_o(1 + \chi_{e_1})$ is the real component of the material's electric permittivity, and $\varepsilon_2 = \varepsilon_o\chi_{e_2} + \sigma/\omega$ describes all losses due to the material's polarizable and free charges. The loss in a dielectric primarily comes from the first term, while the loss in a metal primarily comes from the second term. In general, this term is considered the imaginary part of the material's permittivity. This is due to how permittivity is defined in relation to the material's refractive index, detailed below in section 2.5. Equation 2.11 can be incorporated into equation 2.10 to form:

$$\begin{aligned}\frac{\partial^2 W}{\partial t \partial V} = -\frac{1}{4} i\omega \Big(&(\tilde{\varepsilon} - \varepsilon_o)\left(\widetilde{\boldsymbol{E}}_o{}^2 e^{-2i\omega t} + \left|\widetilde{\boldsymbol{E}}_o\right|^2\right) \\ &- (\tilde{\varepsilon}^* - \varepsilon_o)\left(\widetilde{\boldsymbol{E}}_o^*{}^2 e^{+2i\omega t} + \left|\widetilde{\boldsymbol{E}}_o\right|^2\right)\Big)\end{aligned} \tag{2.12}$$

where $\tilde{\varepsilon} = \varepsilon_1 + i\varepsilon_2$ and $\tilde{\varepsilon}^*$ is its complex conjugate. The material system, as per section 2.1, is at steady state, so equation 2.12 is time averaged:

$$\langle \frac{\partial^2 W}{\partial t \partial V} \rangle = \lim_{t_f \to \infty} \frac{1}{t_f} \int_0^{t_f} \left(\frac{\partial^2 W}{\partial t \partial V} \right) dt, \tag{2.13}$$

such that the equation becomes time insensitive with the $e^{-2i\omega t}$ and $e^{+2i\omega t}$ terms falling to zero. This leaves the final equation for the steady state thermal energy generation rate q":

$$q" = \frac{1}{2} \omega \varepsilon_2 \left| \widetilde{\boldsymbol{E}}_o \right|^2. \tag{2.14}$$

with $\varepsilon_2 = \varepsilon_o \chi_{e_2} + \sigma/\omega$, as defined above.

2.5 Complex refractive index

One of the most common constants used to describe the capacity for a material to absorb electromagnetic energy is the imaginary part κ of its complex refractive index $\tilde{n} = n + i\kappa$, and is used for both metals and dielectrics [44]. This can be seen by expanding equation 2.9 to explicitly show how the guided sinusoidal field evolves as it travels in the z direction:

$$\widetilde{\boldsymbol{E}} = \boldsymbol{E}_1 e^{i(\tilde{k}z - \omega t)} \tag{2.15}$$

where $\boldsymbol{E}_1$ now describes the field's modal distribution in the x- and y-directions, $\tilde{k} = 2\pi\tilde{n}/\lambda_o$ is the complex wavenumber of the field inside the material for a vacuum wavelength λ_o, and ω is the angular frequency of the field. Substituting the complex refractive index into equation 2.15 gives a term $e^{-2\pi\kappa z/\lambda_o}$, causing exponential decay as the wave travels in the z-direction when κ is greater than zero, ie. there is absorption in the material.

A nonmagnetic material's refractive index is related to its permittivity $\tilde{\varepsilon}$ by the equation:

$$\tilde{\varepsilon} = \tilde{n}^2 \varepsilon_o = (n + i\kappa)^2 \varepsilon_o. \tag{2.16}$$

More specifically, the complex permittivity's real and imaginary parts become:

$$\varepsilon_1 = (n^2 - \kappa^2)\varepsilon_o \text{ and } \varepsilon_2 = 2n\kappa\varepsilon_o. \quad (2.17)$$

Both metals and dielectrics therefore have a value for the complex permittivity, even if the polarization and absorption mechanisms differ between bound and free charges.

2.6 Absorption coefficient

A material's ability to absorb electromagnetic waves can also be described by its absorption coefficient α. This term specifically shows how a guided wave's intensity I exponentially decays when propagating in the z direction, via Beer's Law:

$$I = I_o e^{-\alpha z}, \quad (2.18)$$

where I_o is the wave's intensity at position $z = 0$. Since I is directly proportional to $\left|\tilde{\boldsymbol{E}}\right|^2$, the decay terms in equations 2.15 and 2.18 are related by:

$$\alpha = \frac{4\pi\kappa}{\lambda_o}. \quad (2.19)$$

Equations 2.17 and 2.19 can be used to convert between the different absorption parameters obtained from various references.

2.7 Summary

This chapter formulated the essential equations for determining the steady state absorption of light waves into their guiding structures, and the resulting shift in a material's refractive index due to the change in its temperature. In addition, several conversions between material absorption parameters were described. Simulations performed in Chapter 3 will use these equations to explore the thermo-optic behaviour of the SU-8 hybrid plasmonic waveguide material system.

3 Device Design and Simulation

The structure of the hybrid plasmonic waveguide allows for high confinement of the field in a dielectric near the metal layer, while improving the propagation length of the waveguide compared to a pure plasmonic waveguide. This chapter will summarize the design of the SU-8 hybrid plasmonic waveguide and resonator.

In addition, this chapter displays the numerical methods used to simulate the temperature inside a cross-section of the SU-8 hybrid plasmonic waveguide as light propagates through it. First, commercial software, specifically the RF module of COMSOL, is used to find the field distributions inside the hybrid plasmonic waveguide. These distributions are used to create the heat source for the heat conduction equation, in which the temperature of the waveguide is then solved for numerically using the Matlab programming environment. Similar steps are taken for a standard SU-8 photonic waveguide. The comparison between the two material structures will show that the thermo-nonlinearity in the waveguide is expected to increase due to the presence of plasmonic interaction. Part of the work in this chapter is updated from [45].

3.1 Device design

The hybrid plasmonic waveguide structure explored in this work consists of a 1.8 μm × 2μm SU-8 core on top of a 100nm silicon dioxide (SiO_2) gap layer and a 50nm gold (Au) metal layer. These layers are deposited over a 4μm SiO_2 buffer layer and a Si substrate. Figure 3.1 shows a cross-section of this structure. The plasmonic waveguide is butt-coupled to photonic waveguides on either end, the structures of which only differ from the plasmonic waveguide by the absence of the metal layer. The photonic waveguides allows transmission from the laser source, through the plasmonic device, and to the detector with minimal loss. As the confinement in the photonic waveguide is relatively low, a thick SiO_2 buffer layer is required to keep the light from being coupled into the silicon substrate.

The device being explored consists of an all-pass microring resonator coupled from the waveguide in the hybrid plasmonic structure via a MMI coupler. The use of a resonator allows power to build up inside the ring. This, in turn, results in a larger temperature increase and refractive index shift than

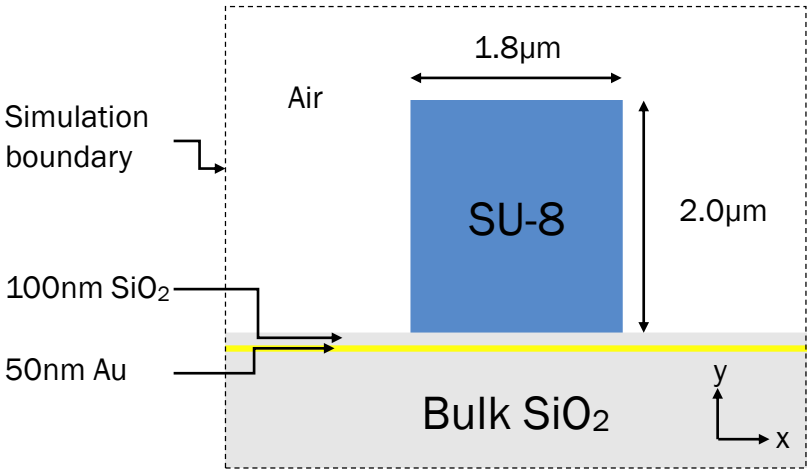

Fig. 3.1: Cross-section and FEM computational domain of SU-8 hybrid plasmonic waveguide. The analogous photonic waveguide has the same structure, without the gold layer.

would otherwise be the case for other types of phase-sensitive structures such as Mach-Zehnder interferometers. The MMI coupler allows power transfer to and from the ring where an evanescent coupler would be inefficient due to the high confinement of the wave inside the waveguide.

The use of a spin-on polymer with good optical transmission properties like SU-8 as the waveguide core at the top of the layer design allows for a simplified fabrication process. For the plasmonic section itself, there are only four deposition steps and two material removal steps, none of which require precise placement. In addition, there are no additional steps required for the photonic sections of the device. As the focus of this work is in exploring nonlinear phenomena and not on the device itself, a device with simple design characteristics is ideal. Details of fabrication for this device are included in Chapter 4.

3.2 Modelling the electric field distribution

The electric fields of the fundamental TE and TM modes in the waveguide cross-sections were computed using the modesolver in COMSOL Multiphysics RF Module. This software uses the finite element method (FEM) to numerically solve the Helmholtz wave equation, which discretizes the computational domain using a mesh that can be dynamically scaled as needed for the feature sizes within the domain. This advantage would be quite useful for efficiently simulating the SU-8 hybrid plasmonic structure, as the thin metal layer is several times smaller than the other dielectric layers. However, the simulation developed in Matlab to solve the heat equation uses the finite difference method (FDM), which requires a pre-set, uniform mesh. As such,

the modesolver domain takes the form of a rectangular grid with 50nm wide by 10nm tall spacing. The structures simulated follow the design as shown to scale in figure 3.1, using the refractive index properties in table 3.1. The silicon substrate is far enough below the waveguide that it can be safely ignored in the simulation. The computational domain was set to have perfectly matched layer boundary conditions, placed at a distance such that the mode is undisturbed.

Table 3.1: Waveguide material properties at 1550nm

	Refractive Index $n + i\kappa$	Thermal Conductivity K (W/m·K)	Thermo-Optic Coefficient dn/dT (/K)
SU-8 2002	$1.575+2.467 \cdot 10^{-6} i$ [24]	0.30 [46]	$-1.87 \cdot 10^{-4}$/K [24]
100nm SiO_2	1.475	0.90 [47]	$1.28 \cdot 10^{-5}$/K [48]
Bulk SiO_2	1.475	2.0 [46]	$1.28 \cdot 10^{-5}$/K
50nm Au	$0.550+11.5\, i$ [44]	90 [49]	-
Air	1	0.024 [50]	-

The simulations focus on finding the fundamental transverse electric (TE) and transverse magnetic (TM) modes, or more precisely, quasi-TE and –TM modes, since the shape of the waveguide allows for non-zero field components in the direction of propagation. Higher order modes are possible, but it is assumed that they are much more lossy, or aren't easily excitable by the fiber-to-chip coupling method used in the measuring process. The fundamental TM and TE modes are easily excited in the experimental setup, and represent, for the hybrid plasmonic waveguide, the modes with the strongest and weakest plasmonic characteristics in terms of mode confinement, respectively.

Figure 3.2 shows the dominant field components for the two modes (E_y for TM and E_x for TE) in the hybrid plasmonic waveguide and the analogous

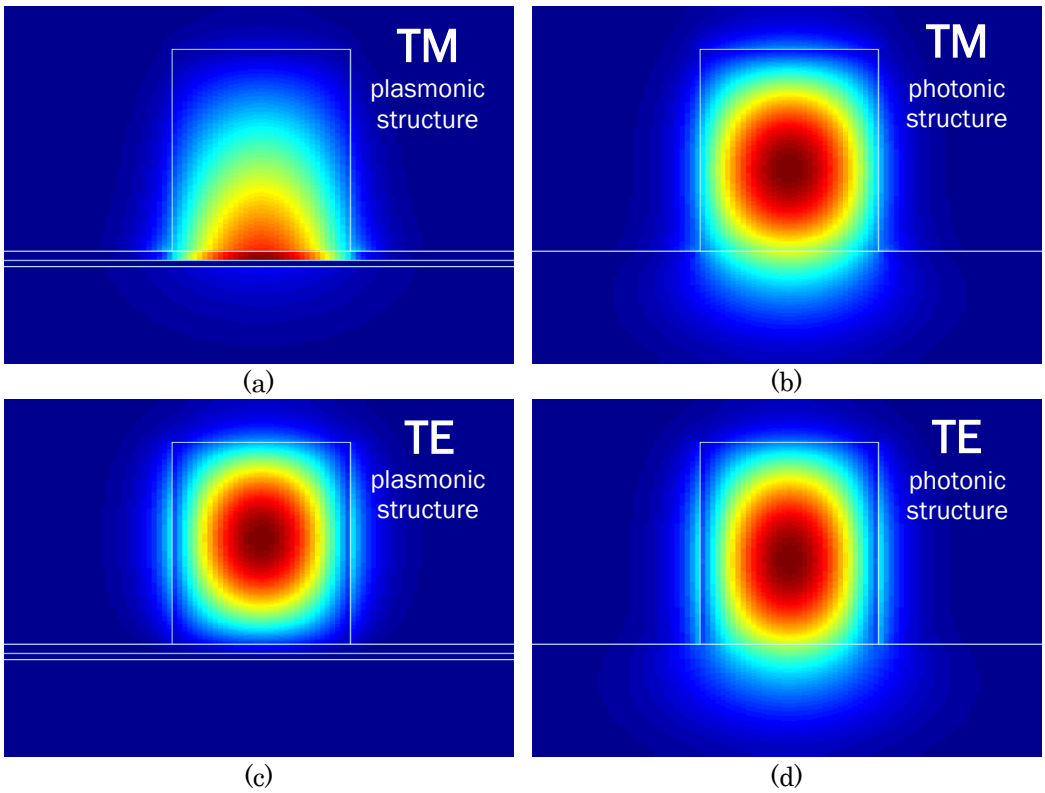

Fig. 3.2: Dominant component of the simulated electric field distribution of the fundamental modes in the chosen structures: E_y component for the TM mode in the (a) hybrid plasmonic structure and (b) photonic structure; E_x component for the TE mode in the (c) hybrid plasmonic structure and (d) photonic structure. (arbitrary units)

photonic waveguide. These field components are the primary contributors to the shape and strength of the heat source in their respective waveguides. The other electric field components (E_x and E_z for TM and E_y and E_z for TE) also contribute, but their effects are much less significant.

As expected for the TM mode in a hybrid plasmonic waveguide, figure 3.2a shows a large percentage of the field strength confined in the SiO_2 layer compared to the other cases, with the highest field strength found at the metal-SiO_2 boundary. In turn, a small but important portion of the field penetrates down into the metal layer. This is likewise the case for the mode's E_x and E_z components. Field exists in the metal layer the TE case, but, as shown in figure

3.2c, since it is concentrated in the centre of the SU-8 layer, its presence in the metal layer is greatly reduced. Note that the TE mode for the hybrid plasmonic structure closely approximates the TE mode in the photonic waveguide, albeit with a much higher confinement in the SU-8 layer.

3.2.1 Simulated propagation length

The modesolver also determines complex effective index of each structure for the given modes. Combining equations 1.1 and 2.18, the propagation length of each case is also calculated, with the assumption that assuming the cross-sections continue as straight waveguides:

$$L_p = \frac{\lambda_0}{4\pi\kappa_{eff}}, \tag{3.20}$$

where κ_{eff} is the imaginary part of the complex effective index. These values allow for comparisons to be made between the theoretical model and the devices fabricated in Chapter 4, as well as how well the structure performs as a waveguide overall.

Table 3.2: Simulated effective index and propagation length for selected structures and modes

Case	Effective index $\tilde{n}_{eff}$	Propagation length L_p (μm)
TM plasmonic	$1.53+1.48\cdot10^{-3}i$	83.31
TE plasmonic	$1.48+4.28\cdot10^{-5}i$	2881
TM photonic	$1.50+4.72\cdot10^{-6}i$	$2.611\cdot10^{4}$
TE photonic	$1.50+4.76\cdot10^{-6}i$	$2.588\cdot10^{4}$

Table 3.2 shows the propagation lengths for the combination of structures and modes simulated above. Note the severe reduction in propagation length for cases with the metal layer. This signifies significant absorption into the metal layer, despite its comparatively small presence in the waveguide. This

implicit high absorption will be further exhibited in section 3.3.

The much shorter propagation length of the TM mode in the hybrid plasmonic waveguide indicates that the power in this case will decline much more quickly than that of the TE mode. As such, given the same input power, devices run in this mode will be exposed to much less internal power than the same device run in the TE mode. These effects will be explored in Chapter 5.

3.3 Waveguide heat source

The modesolver outputs the field components of a wave with arbitrary power. In order to view the effects of the wave as an actual source of heat, the electric field distributions found in section 3.2 are normalized to an optical power of 1mW. The normalized distributions are then transformed with equation 2.14 to calculate the heat source q'' for each waveguide.

As an example, figure 3.3 shows the central y-axis cross-section of the

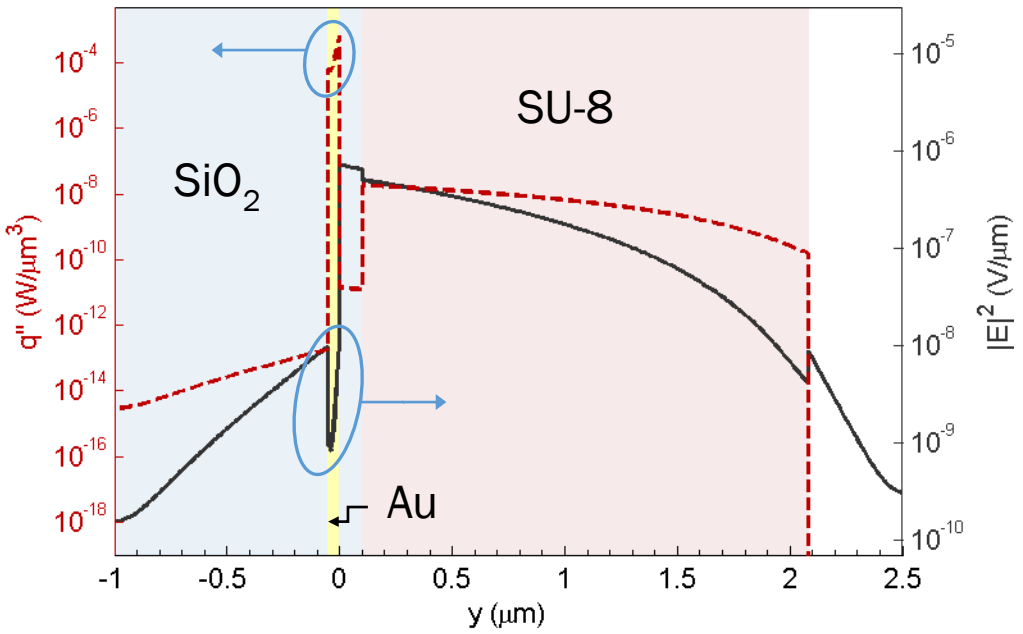

Fig. 3.3: Y-axis cross section of the squared electric field and heat source of the TM mode in the center of the plasmonic waveguide at 1mW optical power.

heat source and electric field for the TM mode of the plasmonic waveguide. For this mode, due to the strong absorption in the metal layer, the source created due to the field inside the metal layer is more than four orders of magnitude greater than the next highest source, even with its correlating electric field being the lowest inside the waveguide. Similarly for the TE mode, the metal is the primary heat source by several orders of magnitude, although much lower compared to the TM case.

The heat sources in the photonic waveguide cases are entirely reliant on absorption in the SU-8 layer, and their profiles inside the waveguide roughly follow the shape of the electric field itself. In addition, a significant portion of the guided field is outside of the waveguide, none of which can contribute to the heat source due to negligible absorption.

3.4 Temperature distribution

After the heat source is created, the resulting steady-state temperature distribution of the waveguide and its surroundings can be determined using equation 2.2 and the field distributions modeled in section 3.2. As stated above, the equation is modeled using FDM, with the same grid parameters as the modesolver simulation, with electric field source normalized to 1mW optical power. The domain is expanded to include the Si substrate underneath the SiO_2 buffer layer, which acts as a heat sink due to its high thermal conductivity of 149 W/m·K. This allows for the bottom boundary condition to be set to a constant temperature of 273K. The other simulation edges have radiating boundary conditions to allow heat to flow freely out of the simulation in those directions.

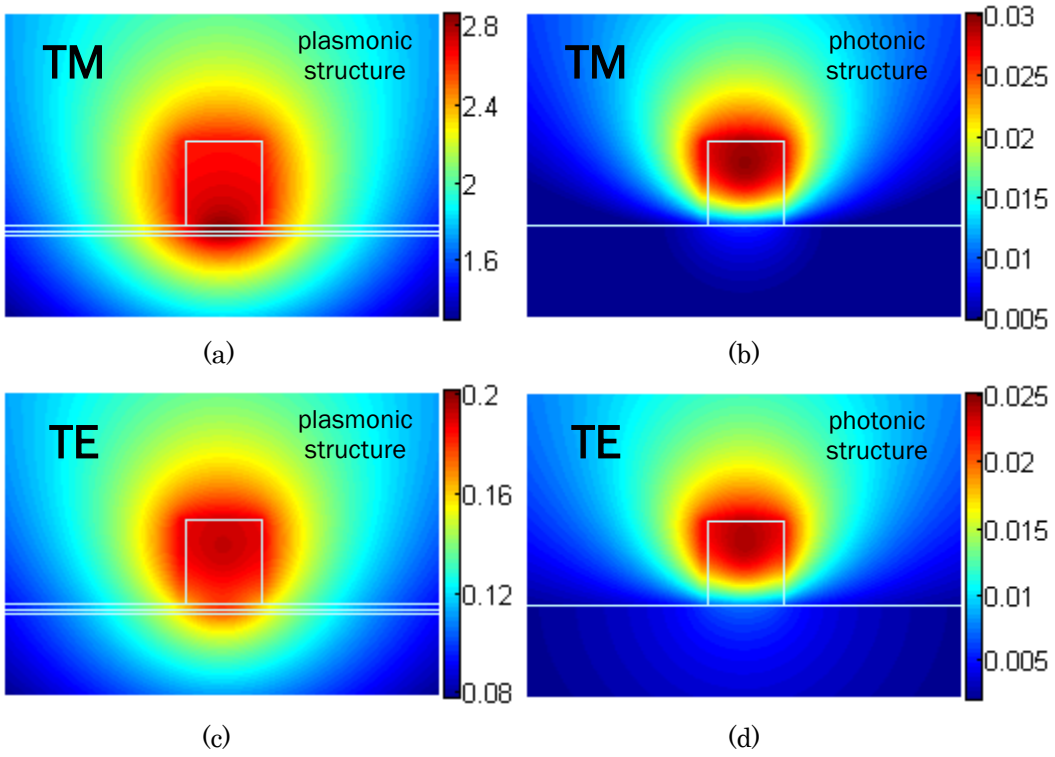

Fig. 3.4: Absolute temperature distribution relative to a base temperature of 273K at 1mW optical power: TM mode in the (a) hybrid plasmonic structure and (b) photonic structure; TE mode in the (c) hybrid plasmonic structure and (d) photonic structure.

With its high thermal conductivity, as shown in table 3.1, the gold layer disperses its heat away from the source, primarily into the SiO_2 buffer layer and Si substrate below. It is expected that any heat that is dispersed towards the waveguide will be largely trapped, due to the low thermal conductivities of the SiO_2 thin film and SU-8 above it. The air surrounding the waveguide will particularly help keep the waveguide insulated. It is assumed that convective heat transfer is minimal.

The results of the thermal simulation are shown in figure 3.4 for all cases. The large heat source in the metal of the hybrid plasmonic waveguide produces a large temperature shift compared to the photonic waveguide for both TE and TM modes. There is also a significant temperature difference between the two

hybrid plasmonic waveguide cases, primarily due to the high field penetration into the metal layer in the TM mode, which the TE mode lacks. The presence of the source at the metal boundary allows relatively uniform heating of the waveguide, as the heat flow is towards the waveguide, and then trapped by the surrounding air. In contrast, with the heat source in the SU-8 for the photonic waveguide, the primary direction of heat flow is into the substrate, and a temperature gradient appears inside the waveguide.

3.5 Effective index shift

The temperature increase in the waveguide results in refractive index shifts in the material layers as per equation 2.1. This leads to an overall change in the waveguide's effective index, as the waves' modes alter to accommodate the change in material index. To show each case's effective index change, the computational domain of the original modesolver simulation from section 3.2 is altered by adding the product of the appropriate temperature distribution and thermo-optic coefficient, shown in table 3.1, and the simulation is run again. This gives a first-order estimation of the shift in effective index. Additional iterations in modeling the relationship between field and temperature distributions will refine the result, although the refinement is minor. A comparison between the results of the two simulations for each case are shown in table 3.3. Δn_{eff} and $\Delta \kappa_{eff}$ are the changes in the

Table 3.3: Change in effective index at 1mW

Case	Peak temperature shift ΔT (K)	Change in effective index	
		Δn_{eff}	$\Delta \kappa_{eff}$
TM plasmonic	2.9	$-4.4 \cdot 10^{-4}$	$+3.84 \cdot 10^{-6}$
TE plasmonic	0.19	$-3.6 \cdot 10^{-5}$	$+4.6 \cdot 10^{-9}$
TM photonic	0.024	$-4 \cdot 10^{-6}$	~0
TE photonic	0.029	$-4 \cdot 10^{-6}$	~0

real and imaginary components of the waveguide's effective index given the temperature increase for each case. The original simulation is assumed to be operating at a power low enough to create negligible amounts of heat.

The primary materials affected by the temperature change are SiO_2 and SU-8, with positive and negative thermo-optic coefficients, respectively. As such, as the temperature of the waveguide increases, the difference in index between the SU-8 and SiO_2 layers will decrease. This leads to a larger proportion of the field propagating inside the thin film SiO_2 layer. Consequently, the imaginary component of the effective index slightly decreases for the photonic waveguides, since SiO_2's κ is lower than SU-8's. However, this increases the loss in the hybrid plasmonic waveguide, as more field penetrates into the gold layer.

The large negative thermo-optic coefficient of SU-8 outweighs the smaller, positive coefficient of SiO_2, and thus there is a negative shift in the real component of the waveguide's effective index for all cases. This will also overwhelm the positive effective index shift resulting from increased waveguide dimensions due to thermal expansion. In the context of the microring resonator explored in Chapter 5, this also results in a negative resonance wavelength shift, as per equation 1.2.

One final note regarding the effect the refractive index shift on the devices' propagation lengths: given that the propagation is influenced by κ_{eff} and this change was minimal, it follows that the change in propagation length is also minimal. Indeed, the shift results in a mere 0.3% reduction for the TM plasmonic case, with the other cases orders of magnitude lower.

3.6 Summary

This chapter has presented the design of an SU-8 hybrid plasmonic waveguide, set up to capitalize on the heat generation prevalent in plasmonic devices. Simulations were then performed to investigate the effects of the heat generation on the waveguide's optical properties. The simulations showed that the minimal penetration into the metal layer still caused a significant temperature increase in the waveguide compared to waveguides lacking the metal layer. This resulted in a notable nonlinear refractive index shift that can be used in resonators to create switching devices.

4 Hybrid Plasmonic Device Fabrication

This chapter describes the general process flow in order to realize the SU-8 hybrid plasmonic structure, following the design from section 3.1. The devices were fabricated in-house at the University of Alberta nanofabrication research facility with the assistance of Nanophotonic Research Laboratory team members Cameron Horvath and Daniel Bachman.

The goal of the fabrication process is to realize plasmonic devices while eliminating lithography mask alignment errors for important layers, specifically the metal layer and waveguide core. Material structures including a silicon core are best utilized using crystalline silicon for its stronger

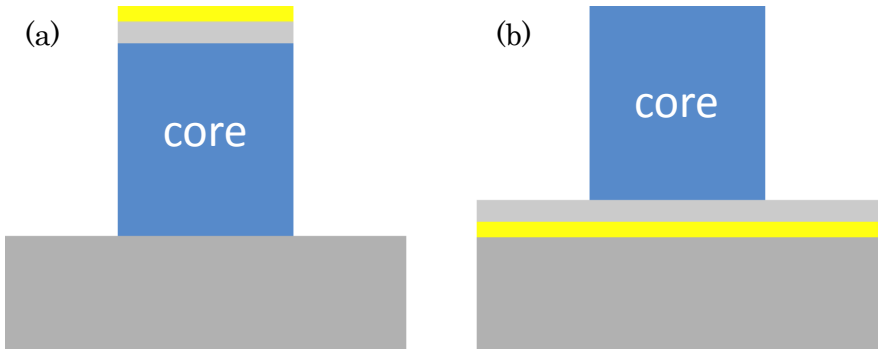

Fig. 4.1: Schematic showing hybrid plasmonic waveguides with metal and gap layers positioned (a) above the waveguide core, and (b) below the waveguide core. Additional processing must occur to remove excess material from the structure in (a).

characteristics over other types; for optical waveguides, this generally means using silicon-on-insulator wafers where the waveguide core layer is already present over an oxide layer. For these structures, the metallic layer must be deposited above the pre-existing core as shown in figure 4.1a, which necessitates precise alignment on the lithography steps and other processes to remove excess material [41, 51]. Depositing the waveguide core on top of the metallic layer, as with this structure, avoids these issues.

The fabrication process steps are shown in figure 4.2. A bare silicon wafer undergoes thermal oxidation to form a 4μm SiO_2 buffer layer. From this wafer, 1x1 cm^2 chips are taken for processing as needed. HPR504 photoresist is then spun, exposed and developed on a chip using UV lithography in order to define the placement of the metallic layer. A thin 50nm gold layer is sputtered onto the chip, after which a lift-off process leaves a large metallic section as desired, with the rest removed. A thin SiO_2 gap layer is formed by PECVD deposition over the entire chip. Finally, the waveguide core layer is created by spinning a 2μm layer of SU-8, and defining the desired device patterns using UV lithography. After developing the SU-8 and cleaning the chip of residue, the chip is manually cleaved to produce an endface for use in the experimental procedure.

The following sections describe in some detail the processes used for the creation of each layer.

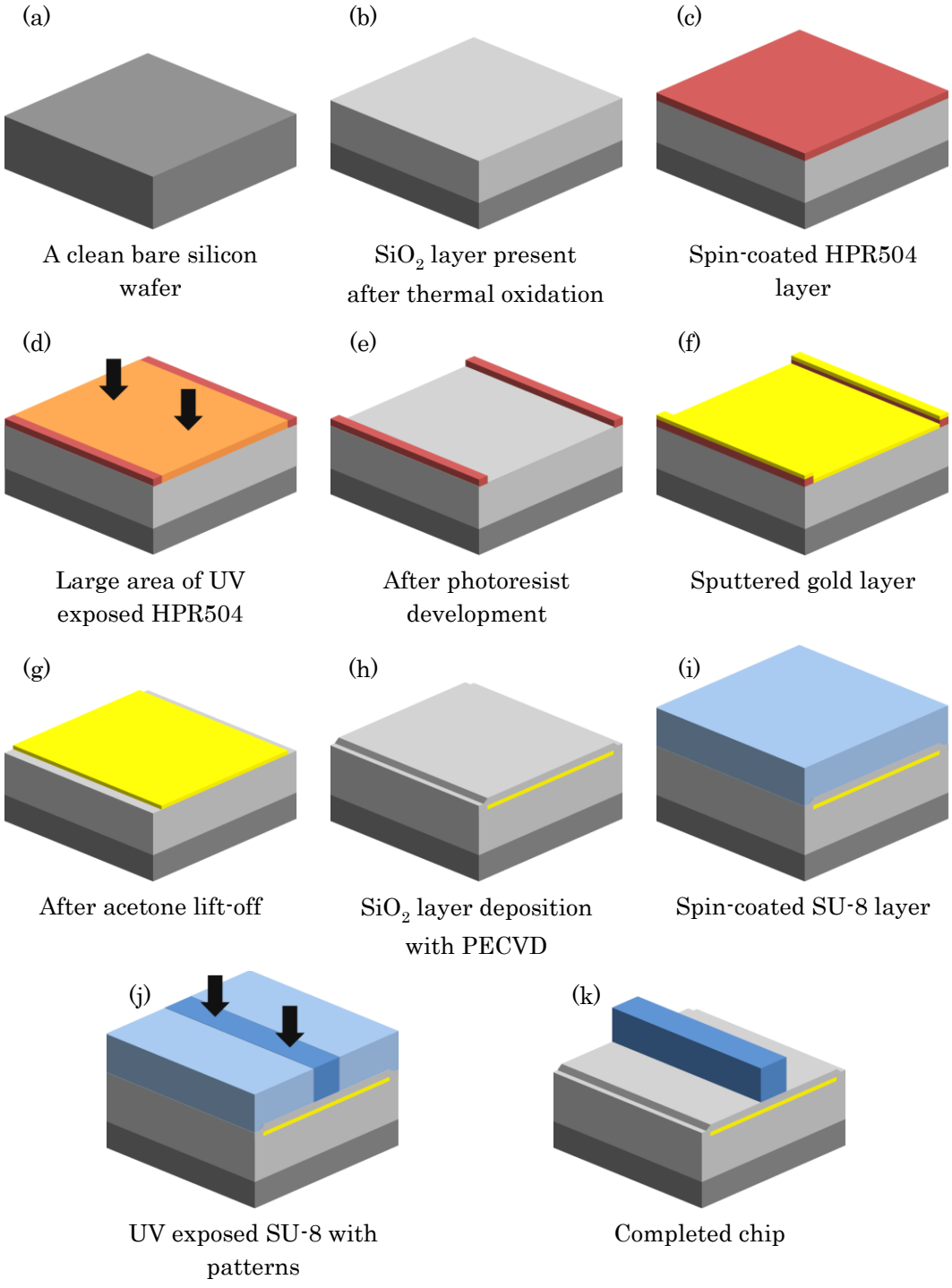

Fig. 4.2: Fabrication process flow for SU-8 hybrid plasmonic devices.

4.1 SiO_2 buffer layer

Fabrication begins with a bare silicon wafer cleaned with a 1:3 mixture of hydrogen peroxide and sulphuric acid, known as Piranha solution. This removes organic residues that would hamper layer deposition. This is the starting condition of the fabrication, illustrated in figure 4.2a.

The first SiO_2 layer was produced via thermal oxidation. The silicon wafer was placed into a MiniBrute furnace heated to 1100°C, with its chamber filled with water vapour. The high temperature allows for the growth of SiO_2 on the wafer as the water chemically reacts with the silicon surface, leaving a hydrogen by-product. As silicon is consumed in the oxidation, the thermal oxide grows into the wafer. The MiniBrute furnace is normally set to grow 1-2µm of thermal oxide over 4-8 hours; several sessions were required to grow the oxide to the desired height of 4µm. Thickness of all layers were monitored via the Filmetrics thickness mapping system. After completion of the thermal oxide growth, the wafers were diced into 1x1 cm^2 chips using a dicing saw. The SiO_2 buffer layer is illustrated in figure 4.2b.

4.2 Gold layer

A 50nm thick strip of gold of varying width was patterned onto the chip via RF sputtering and lift-off. First, a 1.2µm thick layer of HPR504 photoresist was spun onto the chip, then baked to remove leftover solvent. Using a pattern mask and aligner, the photoresist was selectively exposed with ultraviolet (UV) light and then developed. Being a positive photoresist, the portions that were exposed were removed, uncovering the SiO_2 beneath. The gold layer is then deposited using a sputtering system, first 5nm of chrome to promote adhesion

between the gold and SiO_2 layers, then 50nm of gold itself. These procedures are illustrated in figure 4.2c-f.

With the sputtering process being relatively anisotropic, deposition on the sidewalls of the photoresist is relatively low. This allowed for a simple lift-off method to remove the unwanted metal on the photoresist while leaving the gold layer undamaged. This was conducted by immersing the chip in an ultrasonic acetone bath: the acetone dissolving the HP504, and the vibrations stripping it from the SiO_2 substrate. The lift-off is depicted in figure 4.2g.

4.3 SiO_2 gap layer

The second SiO_2 layer was deposited using Plasma Enhanced Chemical Vapor Deposition on a Trion system. 100nm of SiO_2 covers the gold layer in all directions. No extra processing is required. The deposition of this layer is illustrated in figure 4.2h.

4.4 SU-8 waveguide layer

As a negative photoresist, the exposed sections of the SU-8 become insoluble, leaving the excess to be removed with developer. As such, the exposed SU-8 sections form the core for the chip's waveguides and devices.

SU-8 is deposited and processed similarly to HPR504, described in section 4.2. To fulfill the designed height from Chapter 3, SU-8 2002 was selected, and spin-coated at a thickness of 2.4μm. The chip was then baked and exposed with UV. After exposure, a post-exposure bake, and development in SU-8 developer, the unwanted polymer areas are removed. A final hard bake helped anneal any cracks or defects in the layer and remove excess

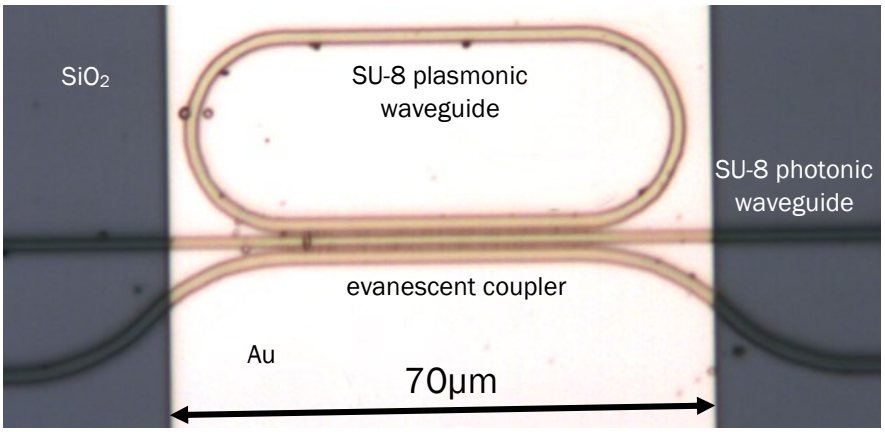

Fig. 4.3: Microscope image of a microring-assisted directional coupler after SU-8 development procedure (before cleaning).

moisture in the resist. Through the multiple bake steps, the SU-8 layer shrank to the desired final thickness of 2.0μm. This series of steps is depicted in figures 4.2i-4.2k.

A microring-assisted directional coupler [52, 53] is shown in figure 4.3 as an example device after development of the SU-8 layer. The racetrack component of the device is easily positioned within the 70μm boundary of the gold strip. The plasmonic device is integrated into the bus waveguides with seamless transitions onto and off of the metal layer. The device is intended to utilize evanescent coupling with a 500nm coupling gap. Unfortunately, due to the high mode confinement inside the waveguide, as described in sections 3.1 and 3.2, it is quickly seen in experiments that any signal entering through a bus waveguide effectively ignores the other components of the device. Since the coupling gap used for this device is near the limit for the UV exposure method available, the device tested in Chapter 5 was designed with the MMI coupler.

4.5 Sample preparation

The 1cm^2 chip is cleaved down to a width of ~300mm to reduce the length of the supporting photonic waveguides on either end of the plasmonic section. This also produces smooth endfaces on the ends of each waveguide, so that lensed fiber tapers can be used to efficiently transfer light into and out of each device, as described below in Chapter 5. A final cleaning with isopropyl alcohol to remove debris allows the chip and its devices to be tested.

Figure 4.4 shows a scanning electron microscope (SEM) image of the cleaved endface of a sample waveguide. The development and baking process has given the waveguide curved corners and slanted sidewalls. These features will result in mode profiles that are slightly distorted from those simulated in section 3.2, altering the confinement of the wave and its interaction with the metal layer. The sidewalls also have a minor ripple along their length, which

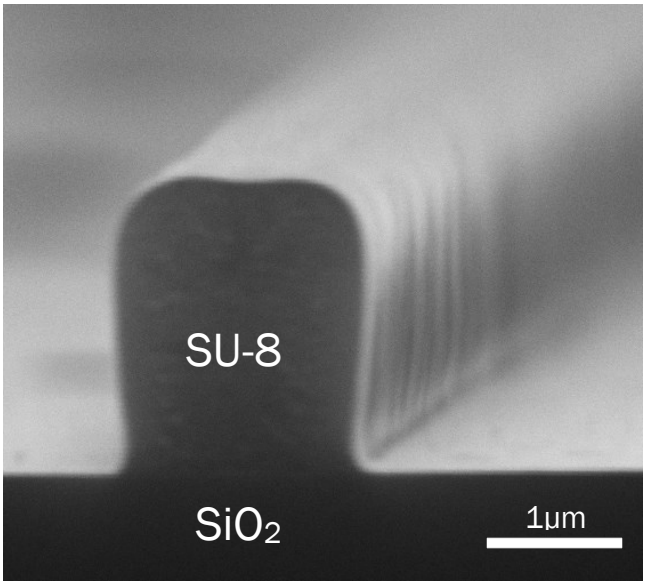

Fig. 4.4:.SEM image of a cleaved edge showing the endface and overall shape of the SU-8 core.

will cause scattering of the wave as it propagates.

4.6 Summary

In this chapter, the procedure to develop SU-8 hybrid plasmonic devices was discussed. The primary feature of this method is the presence of the large metal layer beneath the waveguide core. In this way, device feature complexity is limited only by chosen method to process the SU-8 polymer, as alignment between layers has been simplified to the extreme. While the fabrication method and material discussed limits SU-8 feature sizes to the micron scale, a similar process can be easily developed for different material systems.

The next chapter will use the above fabrication technique to develop a microring resonator to maximize the nonlinear thermal effects discussed in Chapters 2 and 3.

5 Experimental Demonstration of Photothermal Plasmonic Switching

In this chapter, switching is realized and demonstrated in an integrated SU-8 hybrid plasmonic microring resonator. First, sets of plasmonic straight waveguides and microring resonators were fabricated using the process developed in Chapter 4. The characterization of these devices is briefly discussed. A microring resonator was then used as an all-pass filter to demonstrate the effects of thermal nonlinearity on the device's resonance. Finally, switching is achieved using a collinear pump and probe setup with the resonator, demonstrating the opportunity for in-plane integrated plasmonic switching devices. The work from this chapter is updated from [45].

Fabricated devices relevant to this work include plasmonic waveguides with lengths of 10, 30, 70 and 110μm, and a plasmonic microring resonator with outer radius of 25μm coupled to a 70μm plasmonic waveguide. The resonator is shown in figure 5.1, with its couplers labeled. All plasmonic sections are fed through butt couplers to photonic bus waveguides that extend

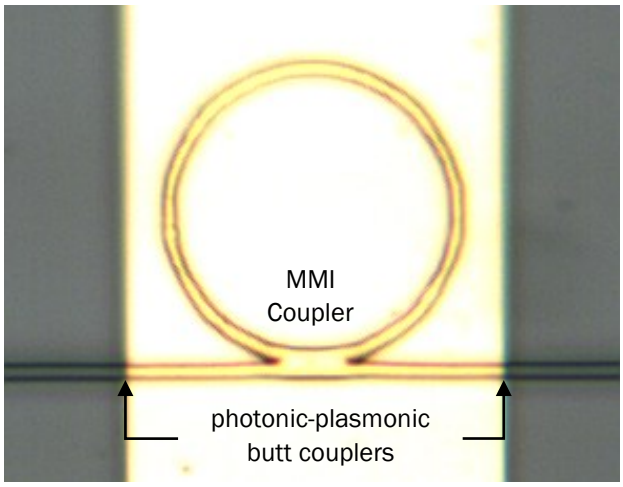

Fig. 5.1: Microscope image of a SU-8 hybrid plasmonic microring resonator with 25μm outer radius.

to the edges of the chip. The microring is connected to the plasmonic bus waveguide via an 11μm long MMI coupler with an average width of 3.6μm. In addition, several photonic waveguides and microrings were created for use as base comparisons, although they are otherwise not characterized.

5.1 Experimental setup

All devices were characterized using the same general setup, with additional equipment included as necessary. The complete schematic with all equipment is portrayed in figure 5.2. Light from a continuous wave (CW) infrared tunable laser is coupled into single mode fiber (SMF) for transportation to and from the measured chip. Piezoelectric motors position the fibers' lensed ends to enable optimum butt coupling with the chip's bus waveguide endfaces.

Waveguide input power is measured by adding a 50/50 fiber coupler after the polarization controller. One output is connected to a power meter, while the other is connected to the stage. Output power is collected with a second power meter. A computer automatically records readings from both power

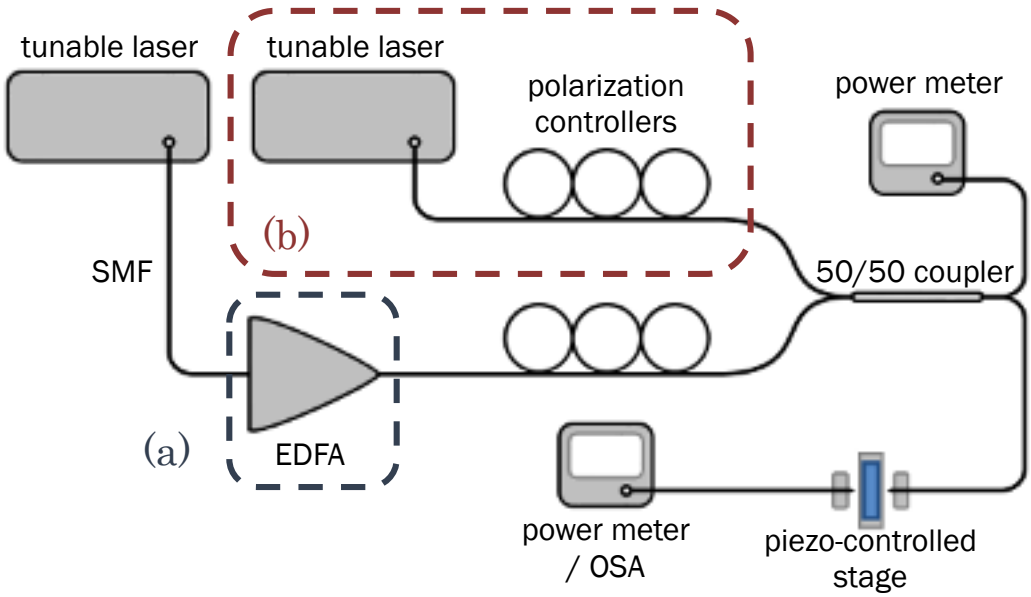

Fig. 5.2: Schematic showing the setup for measuring the spectral response of on-chip devices; a) EDFA included for nonlinear measurements, b) probe branch included for switching measurements.

meters, and automates laser wavelength sweeps as necessary.

To set polarization, the signal is run through a paddle optical fiber polarization controller and then through a polarization crystal. The crystal is positioned on the experiment stage and set to transmit only light with TE or TM polarization as desired. The controller is then manipulated to maximize power through the crystal. With the desired polarization achieved, the crystal is replaced by the chip, while the controller remains in the setup.

The CW lasers used have a maximum power of 20mW, which is not enough to demonstrate a large degree of thermal nonlinearity, given the signal loss that occurs before reaching the device. When higher power is necessary, an erbium-doped fiber amplifier (EDFA) is added to the setup before the polarization controller. The amplifier can output powers in excess of two watts, but it can only amplify wavelengths between 1540-1565nm. This will limit the

microring resonances available for use in the nonlinear measurements.

In order to demonstrate switching, a probe signal is needed in addition to the amplified pump signal, so a second CW laser source is added to the setup. This probe signal is not amplified but does need to be polarized using a second polarizer with the polarization crystal. Once the two signals are separately set to the desired polarization, they are combined using the fiber coupler. The output power meter is switched out for an optical spectrum analyzer (OSA) in order to differentiate the probe signal power from the pump signal power.

5.2 Plasmonic microring resonator characteristics

The propagating mode of interest for this plasmonic resonator is the fundamental TM mode, where the most plasmonic interaction occurs. Conversely, the device's TE mode exhibits the least plasmonic interaction, and, as is readily apparent from the field distributions in figure 3.2, its profile is very close to the TE mode of a photonic device. As such, in order to differentiate the degree of the plasmonic resonator's thermal nonlinearity from that of a photonic device, the resonator's TE mode is used as a quasi-photonic mode. In conjunction with the resonator's TM mode, this enables direct comparisons to be made independent of any peculiarities or defects specific to a separately fabricated photonic device.

Figure 5.3 shows the spectral response of the TE and TM polarizations of the plasmonic microring resonator. With an FSR 9.9nm for the TM mode and 9.8nm for the TE mode, there are two resonances available between 1540nm and 1565nm that can be amplified by the EDFA. The high degree of extinction

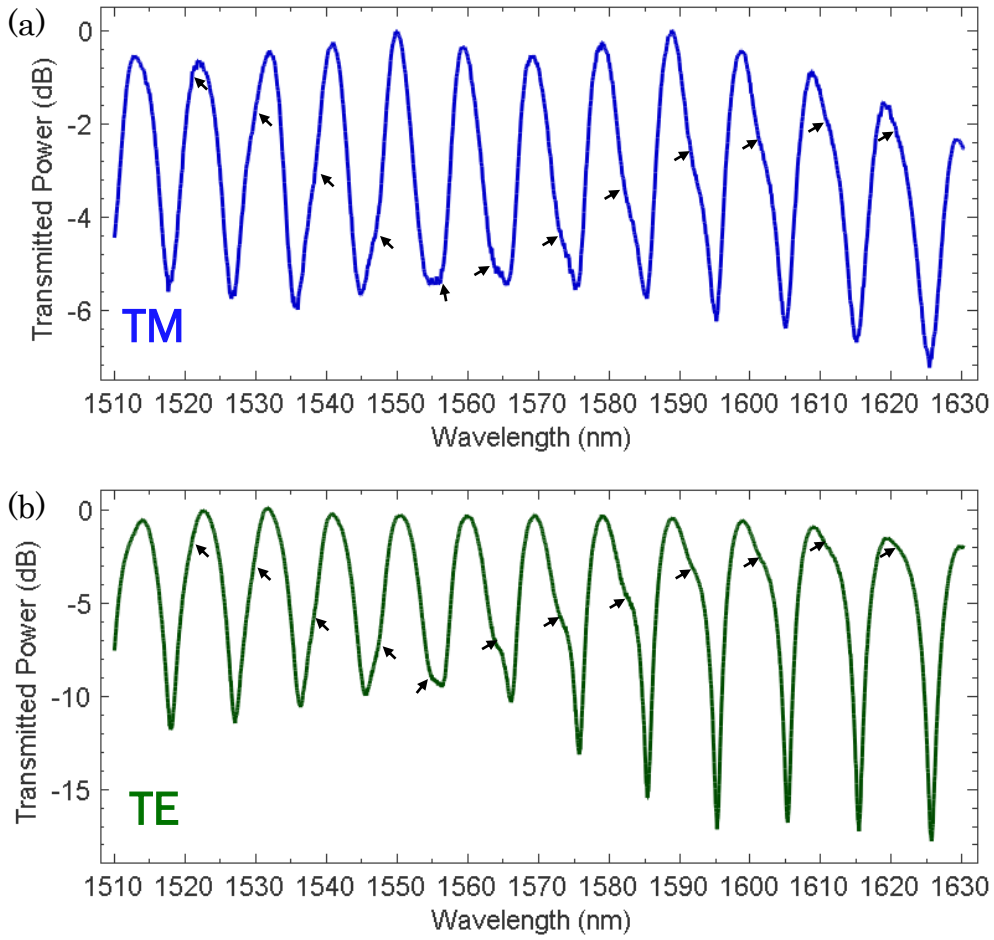

Fig. 5.3: Measured spectral response for the a) TM mode, and b) TE mode in the plasmonic microring. The arrows indicate distortions in the resonances, possibly due to the presence of a higher order mode.

of >10dB indicates from equation 1.4 a closer match between transmission coefficient and roundtrip loss than that of the TM response, with an extinction averaging 5.4dB. This is expected, due the low propagation length of the TM mode traveling through the plasmonic waveguide along the 157μm circumference.

For both polarizations, an additional, possibly higher order, mode with a separate resonance with shorter FSR is visible. The interference of this mode with the fundamental causes distortion in the shape of each overall resonance in addition to widening it.

5.3 Resonator input power and the effect of loss

To get an accurate measure of how the response of the microring resonator changes when exposed to increasing signal power, the resonator input power P_i to be coupled into the ring, must first be determined. Understandably, the power outputted by the laser or amplifier is not the power seen by the resonator, as loss occurs along the input bus waveguide due to absorption and scattering. The setup allows for the direct measurement of the signal power P_f as it approaches the stage, and thus accounts for the loss in the fiber, polarization controller and 50/50 coupler. Sources of loss occurring afterwards must be calculated through other measurements. These sources include: fiber-to-waveguide coupling loss l_f, photonic waveguide propagation loss l_{ph}, photonic-to-plasmonic waveguide coupling loss l_c, and plasmonic waveguide propagation loss l_{pl}. The locations on the device where P_i and these losses are measured are shown in figure 5.4. The values for each of these sources in addition to the total loss to find P_i from a given fiber power are shown in table 5.1, and will be discussed in subsequent sub-sections.

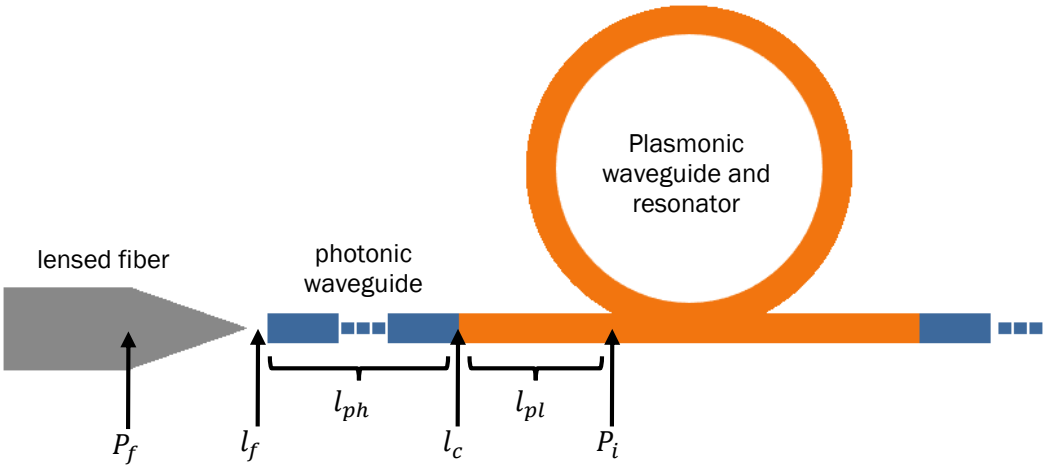

Fig. 5.4: Schematic showing the locations at which losses, the fiber input power P_f, and the resonator input power P_i are calculated.

Table 5.1: Loss in waveguide before ring

Case	Propagation loss (dB)		Coupling loss (dB)		Total loss (dB)
	Photonic l_{ph}	Plasmonic l_{pl}	Fiber - waveguide l_f	Photonic - plasmonic l_c	
TM	−0.327	−2.07	−5.23	−1.26	−8.88
TE	−0.330	−0.0596	−5.23	−0.378	−6.00

The calculation of P_i allows for a measure of the ring's quality independent of any other factors such as bus waveguide length or bus coupler efficiencies. As the MMI coupler is directly involved in the determination of the ring's spectral response, it is considered part of the resonator for these purposes. With this benchmark, the values calculated in this work can be directly used in the design of integrated optical circuits where this resonator is included.

5.3.1 Propagation lengths

A waveguide's propagation length can be quickly converted into a measure of loss in decibels per unit length:

$$\alpha_{L_p} = \frac{-10\log e}{L_p} \text{ [dB/μm]}. \quad (5.1)$$

When multiplied by the relevant waveguide length, the total loss over that distance can be found. The length of the input bus photonic waveguide is 1.47mm, and the plasmonic waveguide is 30μm.

The propagation length of the TM signal through the plasmonic waveguide was calculated using the straight plasmonic waveguides of varying length fabricated above. This involved measuring each of their transmitted powers, then fitting resultant powers to an exponential curve based on waveguide length. The propagation length is extracted as the denominator constant of the exponential fit, as per equation 1.1.

A propagation length of 62μm was calculated at a wavelength of 1550nm [54], for a loss of 2.07dB. The propagation length is 25.3% smaller than the simulated value of 83μm determined in section 3.2. Note that the modesolver assumes a straight waveguide of unchanging dimensions across its length. As shown in figure 4.4, the fabricated waveguide has a moderate amount of roughness along its sidewalls and distorted waveguide shape, which will cause signal scattering. In addition, roughness in the gold layer due the RF sputtering process will both provide additional surface area for plasmonic interaction to occur, as well as contribute further scattering.

The same method can be used to determine the propagation length for other polarizations, and for the photonic structure used in the bus waveguides. However, data is unavailable for these cases. Instead, their theoretical propagation lengths in table 3.2 were reduced by the attenuation found in the plasmonic section. This overcompensates for the loss, as the cases either do not include a metal layer, or interact much less with it. Regardless, the inaccuracy in waveguide loss is minimal. If all the entries in the propagation loss columns except for the measured TM plasmonic entry are replaced with their theoretical values, the resultant increase in P_i is only 1.9% for the TM case and 2.2% for the TE case.

5.3.2 Coupling loss

Several factors contribute to the loss a signal experiences when it couples from one guiding structure to another. A signal leaving the lensed fiber taper on its way to the SU-8 bus waveguide passes through free space, and therefore experiences partial reflection as it travels through the fiber/air interface. In

addition, some percentage of the signal will not couple into the waveguide as the beam emitted from the taper spreads out and does not match the mode of the waveguide. Finally, the signal from the fiber excites several modes inside the waveguide, of which most of the higher-order modes are eventually scattered away. Similar effects occur in the coupler between the plasmonic and photonic waveguides. Here the mismatch between photonic and plasmonic modes becomes the dominant source of loss, while the 50nm mismatch caused by the additional gold layer in the plasmonic waveguide contributes somewhat as well.

The loss a signal experiences as it couples from one guiding structure to another is found by measuring the signal's power output after the coupler and comparing it to the input after discounting the loss caused by other sources. The output fiber's power in P_{out} is related to its input fiber's by:

$$P_{\text{out}} = P_{\text{f}} - 2l_f - 2l_c - l_p \ \text{[dBm]}, \tag{5.2}$$

where l_p is the total propagation loss through the waveguide without couplers. Note that the signal passes through two of each type of coupler before being measured.

For a photonic waveguide, l_c is effectively 0 due to the lack of plasmonic section, and l_p is found using the estimated photonic propagation length above, allowing l_f to be easily calculated for a given power. The fiber coupling loss was found to be effectively independent of both P_i and polarization at l_f = −5.23dB.

The coupling efficiency between the photonic and plasmonic waveguide sections is computed somewhat differently. Given the measured power for

different lengths of plasmonic waveguides, a virtual output power for a 0 length plasmonic waveguide can be estimated. This virtual output power is still influenced by the all the factors in equation 5.2, with l_p again set to be purely photonic and l_f now known. A calculation for TM mode is done in [54], with a resultant $l_c = -1.26$dB. A theoretical value can be obtained by finding the overlap integral of the plasmonic and photonic modes found in section 3.2; the result of −1.20dB fits well with the experimentally obtained value. With data unavailable for the TE mode as discussed in section 5.3.2, the theoretical value of −0.378dB is used for this case.

5.4 Resonance shift due to thermal nonlinearity

The nonlinear resonance shift in the resonator was measured by exposing the resonator to an amplified pump beam of increasing intensity. For each power chosen, the transmission spectrum is recorded for the chosen resonance between the wavelengths of 1540nm and 1550nm. Figure 5.5 shows the resulting blue shift in both TE and TM resonance wavelengths as the power is increased. This coincides with the decrease in the effective index of the waveguide modeled in section 3.5 and the relationship between resonant wavelength and effective index in equation 1.2.

The resonance shifts due to P_i are plotted in figure 5.6, and a linear dependence is found between them. At a shift of −39.91pm/mW, the TM response is 3.6 times greater than that of the TE resonance shift of −11.03pm/mW. While the degree of difference is smaller than that shown in

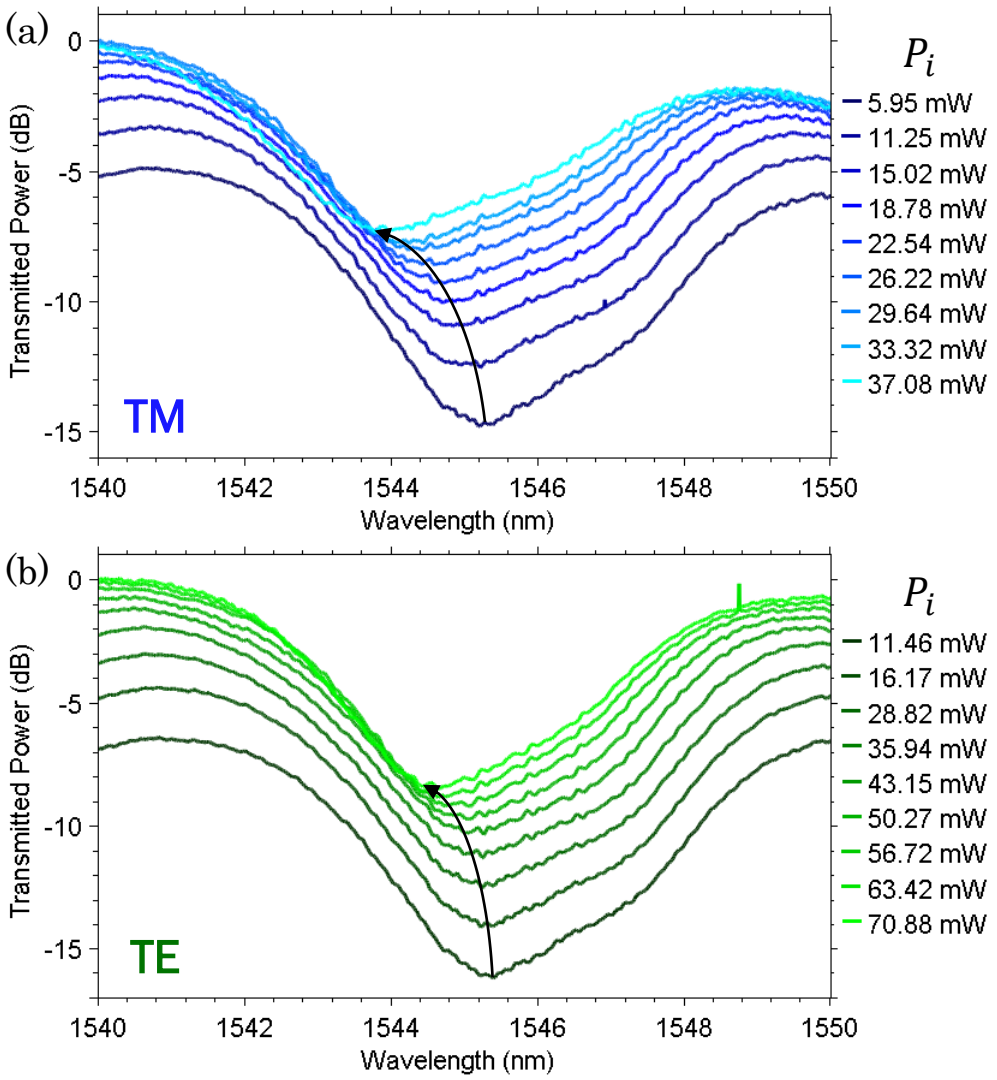

Fig. 5.5: Measured spectral response for the a) TM mode, and b) TE mode in the plasmonic microring at different resonator input powers P_i. Arrows indicate the degree of shift in resonance wavelength with increasing P_i.

figure 3.4, note that the increased absorption with TM polarization that causes the large effective index shift also results in lower absorbable power circulating in the ring. As such, the increased power enhancement in the TE response helps to offset the difference in per-milliwatt heat generation.

A broader comparison can be made to a similar, purely photonic, SU-8 ring resonator, fabricated with a radius of 20μm on the same chip as the

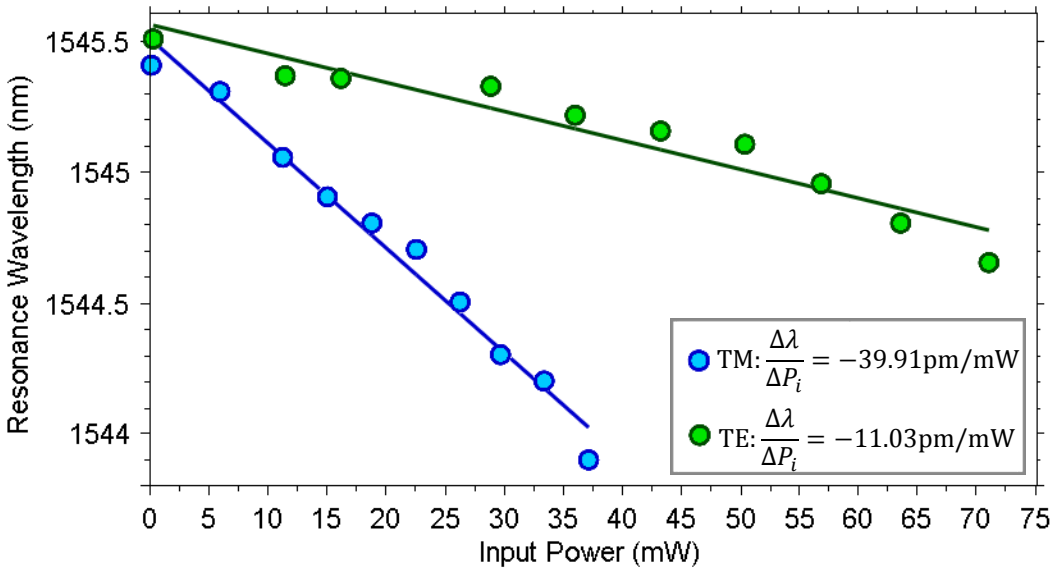

Fig. 5.6: Plasmonic ring resonance wavelength at given resonator input powers P_i for each polarization. The data is fit using linear regression with the least squares method ($R^2 > 0.99$).

plasmonic resonator. It was found to have a resonant wavelength dependence on input power of roughly −1pm/mW, or 40 times smaller than that of the plasmonic resonator. This dependence is in close agreement with results from the measurements of other SU-8 microring resonators [46].

5.5 Demonstration of plasmonic switching

The resonance curve of the microring can be exploited in switching applications, by setting a probe signal with low power at a wavelength near the top of one resonance, and the power-varying pump signal deep in a separate resonance, as shown in figure 5.7. As the resonance experiences a blue-shift with increased pump power, the probe signal wavelength traces the slope of the curve to approach the nearby resonance wavelength and therefore undergoes a drop in power. In this way, a switching device is created such that the probe intensity can be changed from a high state (switch is on) to a low state (switch is off), or vice versa, by changing the intensity of the pump.

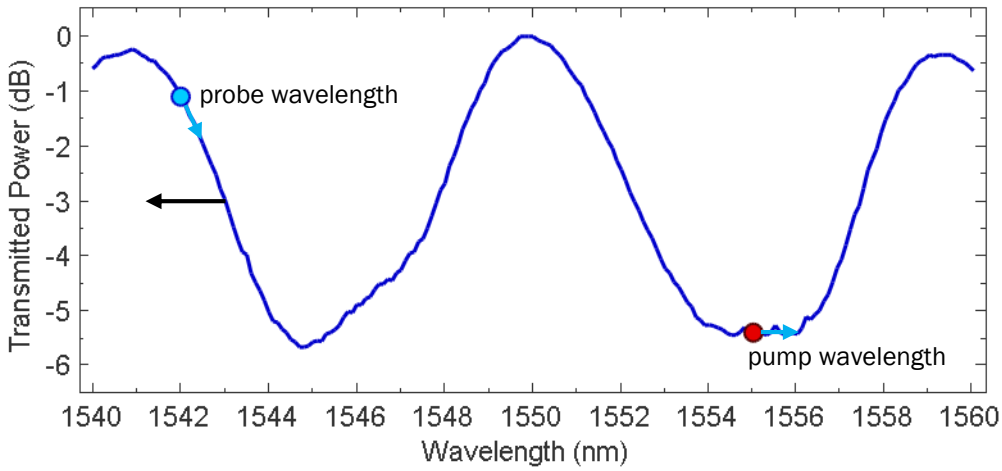

Fig. 5.7: Pump and probe wavelengths displayed on the TM mode spectral response. The black arrow indicates the direction the shape of the response moves along the electromagnetic spectrum as the pump power is increased (blue shift). The light blue arrows indicate the change in position along the response as the response shifts to lower wavelengths.

The probe signal is set to 1542nm near the top of the 1545nm resonance, and the pump signal is set to the 1555nm resonance, and the probe's power is measured as the pump's power is increased. The results are shown in figure 5.8 for TM and TE polarizations. An on-off switching contrast of 3.8dB over a change in input power of 37.2mW is reached for the TM polarization with a switching dependence of −0.10dB/mW. The TE polarization, tested at the same probe and pump wavelengths, drops only 2.3dB over double the input power, resulting in a switching dependence of −0.034dB/mW. The probe wavelength used is not ideal for the TE resonance, as the slope at that point is lower than that of one deeper into the resonance. If moved deeper into the resonance, the TE switching contrast could be improved to as much as 4dB over the same input power.

The drop in probe power is the result of a combination of the resonance shift displayed in section 5.4 and the slope of the resonance used. An

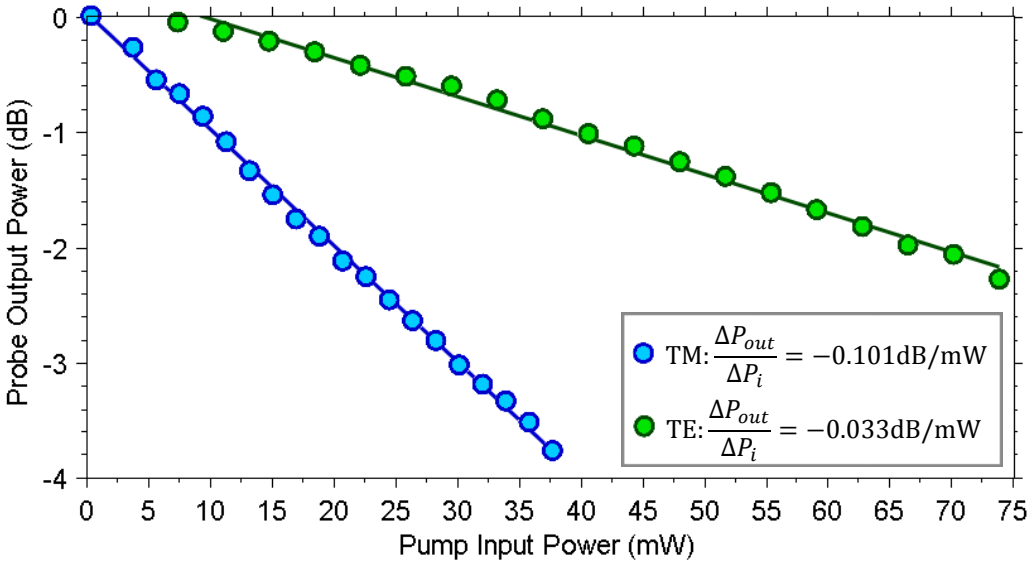

Fig. 5.8: Change in plasmonic probe output power P_{out} at given resonator input powers P_i for each polarization. The data is fit using linear regression with the least squares method ($R^2 > 0.99$).

improvement in the device's extinction ratio will improve the slope: the microring is likely under-coupled, given that its roundtrip loss is much greater than the coupling provided by the MMI coupler. Designing the device with an MMI coupler of increased length, and changing the ring into a racetrack to facilitate the increased coupling length, should improve the resonator characteristics. In addition, replacing the MMI coupler with an evanescent coupler will virtually eliminate the waveguide-to-ring coupling loss, although this will require the replacement of the UV lithography used in section 4.4 with such as electron beam lithography to define the gap required.

5.6 Summary

In this chapter, the thermal nonlinear behaviour of an SU-8 hybrid plasmonic microring resonator was examined. Its resonance spectrum was repeatedly measured using signals of increasing power. With the power absorbed by the waveguide materials, increasing the resonator's temperature

and therefore decreasing its effective index, a blue shift in the resonance spectrum was observed. This resonance shift is an improvement of 40 times that of similar SU-8 photonic ring resonators. The resonance shift was exploited to display switching in the device at a contrast of 0.1dB per milliwatt of the in-plane controlling signal.

6 Conclusions

6.1 Summary of research

In order for plasmonics to become a viable alternative to conventional integrated photonic devices, attention must be paid to the effects of the large loss that is inherent in sub-wavelength confined plasmonic devices. One important consequence of this loss is heat generation, and if not accounted for, devices can experience deviations from their intended functions as the absorbed heat changes material properties. This work focuses on the exploitation of this heat generation to produce photothermal nonlinearities in a plasmonic device for useful applications. Parameters, such as material and device components, were chosen to enhance these effects.

In this thesis, relations between guided wave intensity and the effect on any non-magnetic material's refractive index at steady state were established. The resulting equations are universal in that they can be used with conductors, semi-conductors and dielectrics despite the differences in absorption processes.

Numerical simulations using the established equations were performed to model the heat generation of a sample SU-8 hybrid plasmonic waveguide at telecommunication wavelengths. The thermal simulation modeled the

material components of the waveguide as heat sources due to their absorption of the signal. It was shown that the absorption in the waveguide and hence the amount of heat generated was highly dependent on the polarization of the signal, and were much higher than a purely photonic waveguide of the same materials and dimensions. The resulting shift in the waveguide's effective index due to the thermal nonlinearity was calculated from subsequent simulations.

To experimentally confirm the shift in the waveguide effective index, an all-pass microring resonator was fabricated based on the SU-8 hybrid plasmonic structure. By measuring the spectral response of the resonator as signal power was increased, a shift in resonance wavelength equivalent to the modeled change in waveguide effective index was observed. The plasmonic resonator's resonance was determined to have a 40 times larger dependence on signal power than similar purely photonic microring resonators.

Exploiting the resonance shift with power, the microring resonator then performed as an integrated active switching device, with coplanar pump and probe signals. Varying the pump signal's power controlled the probe signal's position along the shifting spectral response, and consequently its transmitted power. The resonator displayed a contrast of 4dB when its plasmonic mode was excited with less than a third of the power required to get the same contrast with its photonic mode. To the knowledge of the author, this work represents the first demonstration of all-optical active switching with co-propagating signals in a hybrid plasmonic device.

6.2 Future research directions

6.2.1 Maximizing thermal nonlinearity

It was shown in this work that reduced resonator loss and thus improved field enhancement somewhat mitigates the lower resonance shift over maximized absorption, due to increased overall absorbable power inside the ring. Designing a waveguide structure with reduced plasmonic interaction (lowered confinement) and loss with the intention of balancing between relatively high field enhancement and high percentage absorption may result in maximized heat generation.

6.2.2 Thermal response time

This work utilized continuous wave lasers to characterize the fabricated microring resonator, and therefore measured the degree of the device's steady-state thermal sensitivity. However, the speed at which a device reaches steady state is an important characteristic for switching and modulation applications. The thermal response time of a device is relatively slow compared to other switching mechanisms, requiring heat to be transported throughout before steady state can be reached. SU-8 has a very low thermal conductivity, which hinders both the accumulation and dissipation of heat in this device's core.

It was shown that a purely photonic waveguide with SU-8 as the waveguide core had a rise time of ~20μs [46], with presumably a much slower fall time. With this work's device design, a large area of metal is available to transport heat away from the waveguide, allowing for rapid heat dissipation. This dissipation could be improved by thickening the metal layer. The thicker

metal layer has an additional benefit of increasing the propagation length of the waveguide structure [55, 56]. Alternatively, a second layer with even higher thermal conductivity could be added underneath the interacting metal layer, although the additional metal layer might have additional effects on the characteristics of the waveguide structure.

6.2.3 Add drop filters

Positioning a second waveguide on the opposite side of the ring resonator converts the all-pass filter into an add-drop filter. Instead of the original signal being reduced to zero at resonance, it instead exits to the second waveguide. The method used to control the on/off switch in this work could be used in the same way to actively select between the two output ports. With high loss inside the ring, the strength of the signal exiting the second port becomes reliant on coupling between ring and waveguide. The MMI coupler helps with this greatly, and its length can be extended for higher coupling if necessary, although a balance must be made in order to keep the off-resonance through power practical.

6.2.4 Explore faster nonlinearities

Utilizing the hybrid plasmonic structure and microring resonator devices to enhance faster nonlinearities such as two-photon absorption, free carrier dispersion and Kerr nonlinearity, would allow for a greatly expanded variety of switching or modulation-based applications. This would likely require a change in the material system, possibly to a silicon-based core structure as shown in [41]. The main challenge in utilizing these nonlinearities is to reduce or eliminate the strength of the photothermal nonlinear effect such that the

weaker effects aren't overwhelmed. This can be done by using signal speeds that disallow the build-up of heat, or employing an athermal material system [8].

Bibliography

[1] J. A. Davis, R. Venkatesan, A. Kaloyeros, M. Beylansky, S. J. Souri, K. Banerjee, K. C. Saraswat, A. Rahman, R. Reif and J. D. Meindl, "Interconnect Limits on Gigascale Integration (GSI) in the 21st Century," *Proceedings of IEEE,* vol. 89, no. 3, pp. 305-324, 2001.

[2] W. S. Zaoui, A. Kunze, W. Vogel, M. Berroth, J. Butschke, F. Letzkus and J. Burghartz, "Bridging the gap between optical fibers and silicon photonic integrated circuits," *Optics Express,* vol. 22, no. 2, pp. 1277-1286, 2014.

[3] P. Dong, X. Liu, S. Chandrasekhar, L. L. Buhl, R. Aroca and Y.-K. Chen, "Monolithic Silicon Photonic Integrated Circuits for Compact 100+Gb/s Coherent Optical Receivers and Transmitters," *IEEE Journal of Selected Topics in Quantum Electronics,* vol. 20, no. 4, 2014.

[4] "Moving data with silicon and light," Intel, [Online]. Available: http://www.intel.com/content/www/us/en/research/intel-labs-silicon-photonics-research.html. [Accessed 23 March 2015].

[5] "Silicon Integrated Nanophotonics," IBM, [Online]. Available: http://researcher.watson.ibm.com/researcher/view_group.php?id=2757. [Accessed 23 March 2015].

[6] R. Zia, J. A. Schuller and M. L. Brongersma, "Plasmonics: the next chip-scale technology," *Materials Today,* vol. 9, pp. 20-27, 2006.

[7] D. K. Gramotnev and S. I. Bozhevolnyi, "Plasmonics beyond the diffraction limit," *Nature Photonics,* vol. 4, pp. 83-91, 2010.

[8] S. Zhu, G.-Q. Lo, J. Xie and D.-L. Kwong, "Toward Athermal Plasmonic Ring Resonators Based on Cu-TiO2-Si Hybrid Plasmonic Waveguide," *IEEE Photonics Technology Letters,* vol. 25, no. 12, pp. 1161-1164, 2013.

[9] X. Zhu, Q. Li, J. Chan, A. Ahsan, H. L. R. Lira, M. Lipson and K. Bergman, "4 x 44 Gb/s Packet-Level Switching in a Second-Order Microring Switch," *IEEE Photonics Technology Letters,* vol. 24, no. 17, pp. 1555-1557, 2012.

[10] A. M. Prabhu, A. Tsay, Z. Han and V. Van, "Extreme Miniaturization of Silicon Add-Drop Microring Filters for VLSI Photonics Applications," *IEEE Photonics Journal,* vol. 2, no. 3, 2010.

[11] H. Shahoei, D.-X. Xu, J. H. Schmid and J. Yao, "Continuous Slow and Fast Light Generation Using a Silicon-on-Insulator Microring Resonator Incorporating a Multimode Interference Coupler," *Journal of Lightwave Technology,* vol. 32, no. 22, pp. 4279-4284, 2014.

[12] J. Xie, L. Zhou, Z. Zou, J. Wang, X. Li and J. Chen, "Continuously tunable reflective-type optical delay lines using microring resonators," *Optics Express,* vol. 22, no. 1, pp. 817-823, 2014.

[13] F. Liu, Q. Li, Z. Zhang, M. Qiu and Y. Su, "Optically Tunable Delay Line in Silicon Microring Resonator Based on Thermal Nonlinear Effect," *IEEE Journal of Selected Topics in Quantum Electronics,* vol. 14, no. 3, pp. 706-712, 2008.

[14] V. Van, T. A. Ibrahim, P. P. Absil, F. G. Johnson, R. Grover and P.-T. Ho, "Optical Signal Processing Using Nonlinear Semiconductor Microring Resonators," *IEEE Journal of Selected Topics in Quantum Electronics,* vol. 8, no. 3, pp. 705-713, 2002.

[15] Q. Xu and M. Lipson, "Carrier-induced optical bistability in silicon microring resonators," *Optics Letters,* vol. 31, no. 3, pp. 341-343, 2006.

[16] S. Mookherjea and M. A. Schneider, "The nonlinear microring add-drop filter," *Optics Express,* vol. 16, no. 19, pp. 15130-15136, 2008.

[17] S. Feng, T. Lei, H. Chen, H. Cai, X. Luo and A. W. Poon, "Silicon photonics: from a microresonator perspective," *Laser & Photonics Reviews,* vol. 6, no. 2, pp. 145-177, 2012.

[18] A. Chen, "Microresonator Sensors Made in Polymers with Functional Chromophore Dopants," in *Advanced Photonic Structures for Biological and Chemical Detection*, New York, Springer-Verlag, 2009, pp. 7-34.

[19] J. Hu, L. Li, H. Lin, P. Zhang, W. Zhou and Z. Ma, "Flexible integrated photonics: where materials, mechanics and optics meet," *Optical Materials Express,* vol. 3, no. 9, pp. 1313-1331, 2013.

[20] R. J. Ram and K. Lee, "Optical Waveguides for Microfluidic Integration," in *LEOS Annual Meeting Conference Proceedings*, Belek-Antalya, 2009.

[21] O. Castany, K. Sathaye, A. Maalouf, M. Gadonna, I. Hardy and L. Dupont, "Polymer waveguides featuring isotropic and anisotropic sections: Application to the fabrication of polarization splitters," *Optics Communications,* vol. 290, pp. 80-86, 2012.

[22] S. Aithal, S. Aithal and G. Bhat, "Optical Nonlinearity of Dye-doped Polymer Film using Z-scan Technique," in *IEEE 2nd International Conference on Photonics*, Kata Kinabalu, 2011.

[23] J.-C. Weeber, K. Hassan, L. Saviot, A. Dereux, C. Boissière, O. Drupthy, C. Chaneac, E. Burov and A. Pastouret, "Efficient photo-thermal activation of gold nanoparticle-doped polymer plasmonic switches," *Optics Express,* vol. 10, no. 25, pp. 27636-27649, 2012.

[24] K. K. Tung, W. H. Wong and E. Y. B. Pun, "Polymeric optical waveguides using direct ultraviolet photolithography process," *Aplied Physics A,* pp. 621-626, 2005.

[25] K.-J. Baeg, M. Caironi and Y.-Y. Noh, "Toward Printed Integrated Circuits based on Unipolor or Ambipolar Polymer Semiconductors," *Advanced Materials,* vol. 25, no. 31, pp. 4210-4244, 2013.

[26] A. Boersma, S. Wiegersma, B. J. Offrein, J. Duis, J. Delis, M. Ortsiefer, G. van Steenberge, M. Karpinen, A. van Blaaderen and B. Corbett, "Polymer-based optical interconnects using nanoimprint lithography," in *Optoelectronic Interconnects XII*, San Francisco, 2013.

[27] "SU-8 2000 Permanent Epoxy Resists," 2015. [Online]. Available: http://www.microchem.com/Prod-SU82000.htm. [Accessed 23 October 2014].

[28] P. Abgrall, V. Conedera, H. Camon, A.-M. Gue and N.-T. Nguyen, "SU-8 as a structural material for labs-on-chips and microelectromechanical systems," *Electrophoresis,* vol. 28, no. 24, pp. 4539-4551, 2007.

[29] T. Sikanen, S. Tuomikoski, R. A. Ketola, R. Kostiainen, S. Franssila and T. Kotiaho, "Characterization of SU-8 for electrokinetic microfluidic applications," *Lab on a Chip,* vol. 5, no. 8, pp. 888-896, 2005.

[30] C.-Y. Chang, Y. Takahashi, T. Murata and T. Matsue, "Entrapment and measurement of a biologically functionalized microbead with a microwell electrode," *Lab on a Chip,* vol. 9, no. 9, pp. 1185-1192, 2009.

[31] L. Jin, X. Fu, B. Yang, Y. Shi and D. Dai, "Optical bistability in a high-Q racetrack resonator based on small SU-8 ridge waveguides," *Optics Letters,* vol. 38, no. 12, pp. 2134-2136, 2013.

[32] S. A. Maier, Plasmonics: Fundamentals and Applications, Springer, 2007, pp. 21-37.

[33] H. Raether, Surface Plasmons on Smooth and Rough Surfaces and on Gratings, Springer Berlin Heidelberg, 1988, pp. 4-39.

[34] P. Berini, "Long-range surface plasmon polaritons," *Advances in Optics and Photonics,* vol. 1, pp. 484-588, 2009.

[35] G. Veronis and S. Fan, "Guided subwavelength plasmonic mode supported by a slot in a thin metal film," *Optics Letters,* vol. 30, no. 24, pp. 3359-3361, 2005.

[36] Z. Han, A. Y. Elezzabi and V. Van, "Experimental realization of subwavelength plasmonic slot waveguides on a silicon platform," *Optics Letters,* vol. 35, no. 4, pp. 502-504, 2010.

[37] F. Zhou, Y. Liu and W. Cai, "Widely tunable SPP bandgap in a nonlinear metal-insulator-metal waveguide," *Optics Express,* vol. 22, no. 24, pp. 29382-29387, 2014.

[38] S. Sederberg, V. Van and A. Y. Elezzabi, "Monolithic integration of plasmonic waveguides into a complimentary metal-oxide-semiconductor- and photonic-compatible platform," *Applied Physics Letters,* vol. 96, p. 121101, 2010.

[39] A. V. Krasavin and A. V. Zayats, "Passive photonic elements based on dielecctric-loaded surface plasmon polariton waveguides," *Applied Physics Letters,* vol. 90, p. 211101, 2007.

[40] R. Salvador, A. Martínez, C. García-Meca, R. Ortuño and J. Martí, "Analysis of Hybrid Dielectric Plasmonic Waveguides," *IEEE Journal of Selected Topics in Quantum Electronics,* vol. 14, no. 6, pp. 1496-1501, 2008.

[41] M. Wu, Z. Han and V. Van, "Conductor-gap-silicon plasmonic waveguides and passive components at subwavelength scale," *Optics Express,* vol. 18, no. 11, pp. 11728-11736, 2010.

[42] D. J. Thomson, Y. Hu, G. T. Reed and J.-M. Fedeli, "Low Loss MMI Couplers for High Performance MZI Modulators," *IEEE Photonics Technology Letters,* vol. 22, no. 20, pp. 1485-1487, 2010.

[43] A. Yariv, "Universal relations for coupling of optical power between microresonators and dielectric waveguides," *Electronic Letters,* vol. 36, no. 4, pp. 321-322, 2000.

[44] E. Palik, Handbook of Optical Constants of Solids, vol. I, Elsevier, 1998, p. 294.

[45] D. Perron, M. Wu, C. Horvath, D. Bachman and V. Van, "All-plasmonic switching based on thermal nonlinearity in a polymer plasmonic microring resonator," *Optics Letters,* vol. 36, no. 14, pp. 2731-2733, 2011.

[46] L. Yang, D. Dai, J. He and S. He, "Observation of the thermal nonlinear optical effect in a microring resonator based on a small SU-8 polymer ridge optical waveguide," *Proceedings of SPIE-OSA-IEEE Asia Communications and Photonics,* vol. 7631, p. 76310B, 2009.

[47] T. Yamane, N. Nagai, S.-I. Katayama and M. Todoko, "Measurement of thermal conductivity of silicon dioxide thin films using a 3ω method," *Journal of Applied Physics,* vol. 91, no. 12, pp. 9772-9776, 2002.

[48] A. K. Sharma and B. D. Gupta, "Influence of temperature on the sensitivity and signal-to-noise ratio of a fiber-optic surface-plasmon resonance sensor," *Applied Optics,* vol. 45, no. 1, pp. 151-161, 2006.

[49] J.-P. Bourgoin, G.-G. Allogho and A. Haché, "Thermal conduction in thin films measured by optical surface thermal lensing," *Journal of Applied Physics,* vol. 108, p. 073520, 2010.

[50] J. Lienhard IV and J. Lienhard V, in *A Heat Transfer Textbook*, Cambridge, Phlogiston Press, 2008, p. 714.

[51] J. Kim and S. Park, "The Design and Analysis of Monolithic Integration of CMOS-Compatible Plasmonic Waveguides for On-Chip Electronic-

Photonic Integrated Circuits," *Journal of Lightwave Technology,* vol. 31, no. 18, pp. 2974-2981, 2013.

[52] A. M. Prabhu, V. Van, W. N. Herman and P.-T. Ho, "Compact silicon microring-assisted directional couplers for optical signal processing applications," *Optics Letters,* vol. 34, no. 8, pp. 1249-1251, 2009.

[53] D. Perron, P.-T. Ho and V. Van, "Resonant Power Coupling in Asynchronous Microring-Assisted Directional Couplers," *IEEE Journal of Quantum Electronics,* vol. 46, no. 12, pp. 1709-1716, 2010.

[54] C. Horvath, D. Bachman, M. Wu, D. Perron and V. Van, "Polymer Hybrid Plasmonic Waveguides and Microring Resonators," *IEEE Photonics Technology Letters,* vol. 23, no. 17, pp. 1267-1269, 2011.

[55] A. Kolomenski, A. Kolommenskii, J. Noel, S. Peng and H. Schuessler, "Propagation length of surface plasmons in a metal film with roughness," *Applied Optics,* vol. 48, no. 30, pp. 5683-5691, 2009.

[56] M. Wu, "Silicon Hybrid Plasmonic Waveguide and Passive Devices," M.S. Thesis, Department of Electrical Engineering, University of Alberta, Edmonton AB, Canada, 2011.